

# Surface instability in a nematic elastomer

Morgan Barnes,<sup>1</sup> Fan Feng,<sup>1</sup> and John S. Biggins<sup>1,\*</sup>

<sup>1</sup>*Department of Engineering, University of Cambridge, Trumpington St., Cambridge CB2 1PZ, United Kingdom*

(Dated: March 20, 2023)

Liquid crystal elastomers (LCEs) are soft phase-changing solids that exhibit large reversible contractions upon heating, Goldstone-like soft modes and resultant microstructural instabilities. We heat a planar LCE slab to isotropic, clamp the lower surface then cool back to nematic. Clamping prevents macroscopic elongation, producing compression and microstructure. We see that the free surface destabilizes, adopting topography with amplitude and wavelength similar to thickness. To understand the instability, we numerically compute the microstructural relaxation of a “non-ideal” LCE energy. Linear stability reveals a Biot-like scale-free instability, but with oblique wavevector. However, simulation and experiment show that, unlike classic elastic creasing, instability culminates in a cross-hatch without cusps or hysteresis, and is constructed entirely from low-stress soft modes.

Keywords: Nematic elastomer, instability, Biot, creasing, microstructure, laminate, soft-mode

Liquid crystal elastomers (LCEs) are actuating solids that recall the dramatic shape transformations of biological tissues. Microscopically, LCEs are cross-linked networks of LC polymers [1]. Actuation occurs via the isotropic-nematic phase transition, which biases polymers along the director, generating large elongations on cooling, and muscular contraction on heating [2, 3]. Furthermore, LCEs can be fabricated with spatial director profiles to allow complex morphing [4] such as a cone [5, 6] or face [7, 8], mimicking the differential growth that underpin morphogenesis [9]. Symmetry breaking during the isotropic-nematic transition also endows nematic LCEs with Goldstone-like “soft-modes” in which large deformations induce director rotation at almost zero energy/stress [10, 11]. Such modes enable actuation by modest electric fields [12, 13] and generate martensite-like [14] microstructural instabilities [15–17]. However, despite progress in idealized cases [17–19], we still lack a realistic coarse-grained constitutive model for LCEs that accounts for soft modes and microstructure, preventing the analysis of macroscopic samples under load.

Compressive mechanical instabilities like buckling provide an attractive additional route to complex shape change, without needing pre-patterning. For example, the ubiquitous Biot creasing instability [20–23] occurs at the free surface of soft solids under compression, and sculpts cusped folds [22], including biological villi [24] and brain sulci [25]. Here, we tackle the analogous problems in nematic LCEs, where the consequences of compression are enriched and modified by soft modes and microstructure. Experimentally, we find a different cusp-free surface instability with a cross-hatch pattern. In pursuit of theoretical/numerical insight, we then develop a realistic 3D LCE continuum model by numerical relaxation of a “non-ideal” energy [26], enabling multi-scale simulations and stability analysis that capture the key features.

Our experiments begin by fabricating a monodomain LCE following the protocol in [8] (SI [27] Sec. I) which

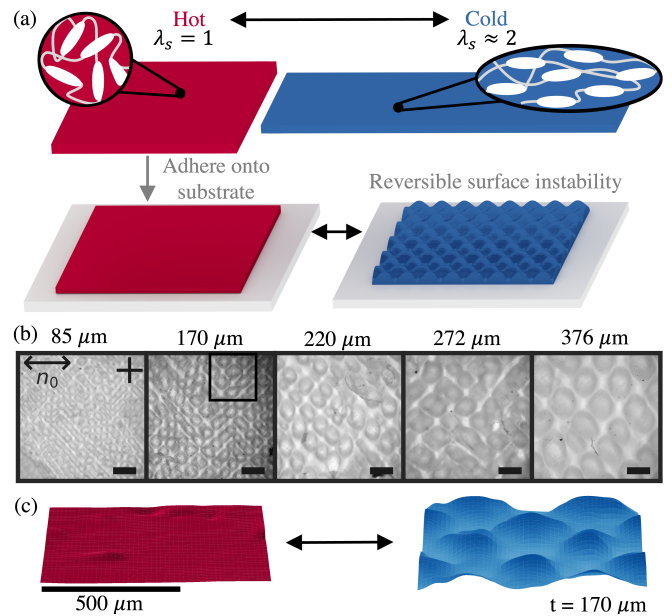


FIG. 1. (a) Schematic of monodomain LCE actuation between hot (isotropic) and cold (nematic) states and the resulting surface instability when adhered to a surface in the hot state. (b) Micrographs (POM) of resulting surface instability for varying LCE thicknesses. Scale bars are  $500\mu\text{m}$ . (c) Representative topography changes from optical profilometry (SI Sec. III), with true aspect ratio, corresponding to the boxed region in (b).

uses a two-step crosslinking method with mechanical programming, as pioneered by Finkelmann [2], but with modern and commercially available acrylate-functionalized reactive mesogens, and thiol functionalized chain extenders and crosslinkers [28]. The result is a rectilinear LCE film that is clear but highly birefringent at room temperature owing to its planar nematic alignment. The film actuates reversibly, with a stretching factor of  $\lambda_s \approx 2$  on cooling from isotropic to nematic (SI Fig. S2). Inspired by creasing of gel slabs that are swollen whilst adhered

to a stiff foundation [21, 23], we then heat the LCE film to the isotropic, adhere it to a glass slide, and cool back to nematic (Fig. 1(a)). The slide prevents macroscopic elongation, placing the LCE in compression. On cooling, the LCE becomes milky, indicating microstructure. Moreover, at room temperature the surface becomes unstable, forming a high amplitude and ordered cross-hatch pattern of topography consisting of relatively wide proud bumps separated by narrow valleys (Fig. 1(b,c), and SI [27] Sec.III, M1, M2). Topography is reversible on heating (SI [27] M3), and experiments varying LCE thicknesses reveal that amplitude and wavelength are simply proportional to slab depth.

The simplest constitutive model for an isotropic elastomer with shear modulus  $\mu$  and subject to deformation gradient  $\mathbf{\Lambda}$  is the neo-Hookean energy density  $W_{NH}(\mathbf{\Lambda}) = \frac{1}{2}\mu\text{Tr}(\mathbf{\Lambda}\mathbf{\Lambda}^T)$ , augmented by the incompressibility constraint,  $\text{Det}(\mathbf{\Lambda}) = 1$ . The energy's minimum is the undeformed state,  $\mathbf{\Lambda} = \mathbf{I}$ . On cooling to the nematic, an LCE undergoes a spontaneous elongation of  $\lambda_s$  along the (unit) director  $\mathbf{n}$ , a spontaneous deformation  $\mathbf{\Lambda}_s(\mathbf{n}) = \lambda_s\mathbf{n}\otimes\mathbf{n} + \lambda_s^{-1/2}(\mathbf{I} - \mathbf{n}\otimes\mathbf{n})$ . If subsequent deformations are neo-Hookean with respect to this new minimizing state, we obtain the energy  $W_{NH}(\mathbf{\Lambda}\mathbf{\Lambda}_s^{-1})$ , which is accordingly minimized by  $\mathbf{\Lambda} = \mathbf{\Lambda}_s$ . Finally, allowing the director to rotate to minimize the elastic energy leads to an energy function depending solely on deformation [17]

$$W_I(\mathbf{\Lambda}) = \frac{1}{2}\mu(\Lambda_1^2\lambda_s + \Lambda_2^2\lambda_s + \Lambda_3^2/\lambda_s^2), \quad (1)$$

where  $\mathbf{\Lambda}$  is deformation gradient from the isotropic state and  $\Lambda_i$  are the ordered principle stretches. This form corresponds to the ‘‘trace formula’’ (with  $\lambda_s = r^{1/3}$ ), originally derived directly from statistical mechanics [1, 29]. The energy is minimized by  $\mathbf{\Lambda} = \mathbf{\Lambda}_s(\mathbf{n})$  for any choice of  $\mathbf{n}$ , giving the expected degenerate set of ground states (Fig. 2(a)).

This *ideal* energy is indeed susceptible to microstructure. For example, consider an isotropic LCE that cools with a director  $\mathbf{n}_0 = \hat{\mathbf{y}}$  and minimizing elongation  $\mathbf{\Lambda}_s(\hat{\mathbf{y}})$ . Clearly the LCE could have formed with  $\mathbf{n} = \hat{\mathbf{x}}$ , so the subsequent deformation  $\mathbf{F} = \mathbf{\Lambda}_s(\hat{\mathbf{x}})\mathbf{\Lambda}_s(\hat{\mathbf{y}})^{-1}$  (corresponding to a stretch by  $\lambda_s^{3/2}$  along  $\hat{\mathbf{y}}$ ) does not cost energy. However, intermediate pure stretches are not soft, as the corresponding soft modes are sheared (Fig. 2(a)). Remarkably, the LCE will accommodate these intermediate states softly by rapidly alternating between bands of shear with alternating sign, (Fig. 2(b)) leading to a laminar ‘‘stripe-domain’’ micro-structure [16] that is geometrically compatible, soft and, with fine bands, macroscopically indistinguishable from that imposed.

More generally, any pure shear can be expressed as  $\mathbf{S}(\boldsymbol{\gamma}, \hat{\mathbf{m}}) = \mathbf{I} + \boldsymbol{\gamma}\otimes\hat{\mathbf{m}}$ , where  $\hat{\mathbf{m}}$  is the shear plane normal, and  $\boldsymbol{\gamma}$ , orthogonal to  $\hat{\mathbf{m}}$ , encodes shearing magnitude and direction. A general laminar shearing micro-structure

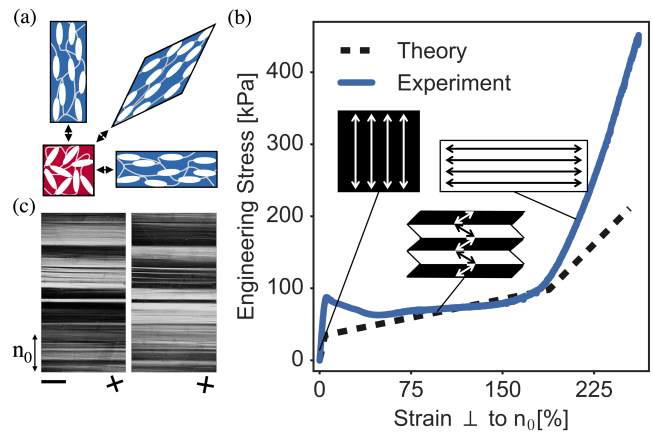


FIG. 2. (a) Soft modes in LCEs. (b) Experimental and theoretical [1] stress-strain curves. Theory parameters:  $\lambda_s = 2, \alpha = 0.05, \mu = 600$  kPa. (c) Micrographs of a stripe domain microstructure rotated under cross-polarizers. Scale bar is  $500\mu\text{m}$ .

that averages to  $\mathbf{\Lambda}$  may thus be constructed as:

$$\begin{aligned} \mathbf{\Lambda} &= f\mathbf{\Lambda}_1 + (1-f)\mathbf{\Lambda}_2 \quad \text{where} \quad (2) \\ \mathbf{\Lambda}_1 &= \mathbf{S}((1-f)\mathbf{a}, \hat{\mathbf{m}})\mathbf{\Lambda}, \quad \text{and} \quad \mathbf{\Lambda}_2 = \mathbf{S}(-f\mathbf{a}, \hat{\mathbf{m}})\mathbf{\Lambda}, \end{aligned}$$

where  $0 < f < 1$  is the volume fraction of  $\mathbf{\Lambda}_1$ . If the resultant energy,  $fW(\mathbf{\Lambda}_1) + (1-f)W(\mathbf{\Lambda}_2)$ , is lower than  $W(\mathbf{\Lambda})$  then microstructure is favoured. For  $W_I(\mathbf{\Lambda})$ , a fully relaxed energy has been analytically constructed [17], with the conclusion that all deformations  $\mathbf{\Lambda}$  with principle stretches less extreme than  $\lambda_s$  may be achieved softly with, at most, double laminates. Since this *quasi-convex hull* contains  $\mathbf{\Lambda} = \mathbf{I}$ , the elastomer can macroscopically accommodate the experimental compression, giving no incentive for surface instability.

The missing physics is non-ideality: a preferred director  $\mathbf{n}_0$  was imprinted in the LCE during fabrication, breaking degeneracy and imposing a small cost on director rotation. Such effects are included in the energy by adding an anchoring term proportional to a small dimensionless non-ideality coefficient  $\alpha$  [26],

$$\begin{aligned} W_{NI}(\mathbf{\Lambda}) &= \min_{\mathbf{n}} (W_{NH}(\mathbf{\Lambda}\mathbf{\Lambda}_s^{-1}(\mathbf{n})) \\ &\quad + \frac{1}{2}\alpha\lambda_s\mu\text{Tr}(\mathbf{\Lambda}(\mathbf{I} - \mathbf{n}_0\otimes\mathbf{n}_0)\mathbf{\Lambda}^T\mathbf{n}\otimes\mathbf{n})). \end{aligned} \quad (3)$$

We may again analytically minimize over  $\mathbf{n}$  by collecting all the  $\mathbf{n}$  containing terms as  $\frac{1}{2}\mu\text{Tr}(\mathbf{M}\mathbf{n}\otimes\mathbf{n})$ , and directing  $\mathbf{n}$  along the eigenvector of  $\mathbf{M}$  with most negative eigenvalue. This energy's microstructural relaxation has been well studied for thin films in tension [16], where single-laminates provide a complete solution [18], but a 3D result remains distant. We thus seek to construct the relaxed energy function numerically. The space of 3D deformations  $\mathbf{\Lambda}$  is nine dimensional, however incompressibility, frame indifference, and

uniaxial material symmetry allow the energy to be written as a function of any four independent scalar invariants [30, 31]. We may thus re-express any nematic energy as  $W(\mathbf{\Lambda}) = w(\Lambda_3, \Lambda_1, \theta, \phi)$ ,  $\theta, \phi$  being the latitude and longitude of  $\mathbf{n}_0$  in the (reference state) principle stretch axes. To compute the relaxed energy, we first construct a grid of  $\sim 50k$  points over this space, spanning  $1 \leq \Lambda_3 \leq 4$  with  $\delta\Lambda_3 = 0.1$  resolution, and with eleven points across each of the remaining three (finite) dimensions. At each point, we then compute a test deformation  $\mathbf{\Lambda}_t(\Lambda_3, \Lambda_1, \theta, \phi)$  matching the invariants, and then, at fixed  $\lambda_s$  and  $\alpha$ , numerically minimize over “rank-1” single laminates:

$$W_{R1}(\mathbf{\Lambda}) = \min_{f, \hat{\mathbf{m}}, \mathbf{a}, \perp \hat{\mathbf{m}}} fW_{NI}(\mathbf{\Lambda}_1) + (1-f)W_{NI}(\mathbf{\Lambda}_2). \quad (4)$$

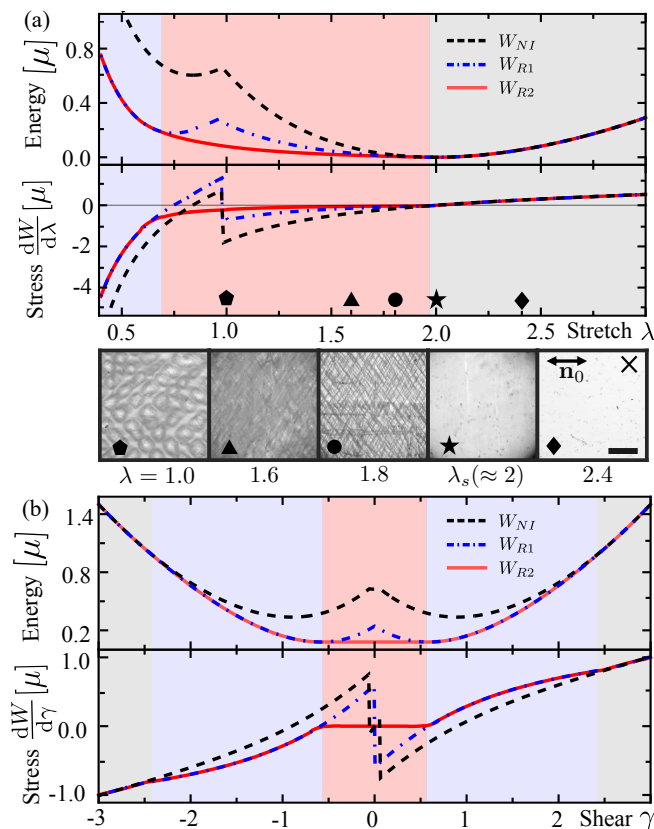


FIG. 3. Energy density and engineering stress upon (a) uniaxial stretch  $\mathbf{\Lambda} = \lambda \mathbf{n}_0 \otimes \mathbf{n}_0 + \lambda^{-1/2}(\mathbf{I} - \mathbf{n}_0 \otimes \mathbf{n}_0)$  and (b) simple shear  $\mathbf{\Lambda} = \mathbf{I} + \gamma(\mathbf{n}_0 \times \mathbf{n}_0^\perp) \otimes \mathbf{n}_0^\perp$ . Gray-shaded domain: no twinning; blue-shaded domain: first-order twin; red-shaded domain: second-order twin. Crossed polar images of samples in (a) bottom showing micro-structure evolution in uniaxial strain.  $\lambda = 1$  shows the surface instability,  $1 < \lambda < \lambda_s$  shows a cross-hatch microstructure, and  $\lambda \geq \lambda_s$  is a clear monodomain.

Minimization over the five scalar lamination parameters in  $(f, \hat{\mathbf{m}}, \mathbf{a})$  is conducted in Mathematica, using simulated annealing and conjugate gradient (detailed algo-

rithm in SI Sec. V [27]). Interpolation of the results on the 4D grid then yields a numerical approximation of  $W_{R1}$  and the lamination parameters. Repeating with  $W_{R1}$  produces  $W_{R2}$ , while, as ideally, further iterations provide no further benefit. Finally, to reveal the full microstructure, we use the  $R1$  lamination parameter interpolation to write the  $R2$  microstructure at each point in terms of its four constituent deformations, and then use these as a starting guess for a conjugate minimization over the full 15 scalar parameters describing both rounds of lamination, using analytic derivatives to ensure strong convergence. The relaxed coarse-grained first Piola-Kirchhoff (PK1) stress for the  $\mathbf{\Lambda}_t$  at each grid point can then be computed as the volume-weighted sum of the constituent stresses, which are themselves evaluated as analytic derivatives  $P_{ij} = \frac{\partial W_{NI}}{\partial \Lambda_{ij}}$  (SI Sec. IV [27]). Interpolating these stresses yields a numerical stress for any  $\mathbf{\Lambda}_t$ , which may be rotated to produce the stress for any  $\mathbf{\Lambda}$ .

In Fig. 3 we show energy-extension and force-extension curves for two simple test cases: uniaxial stretch along  $\mathbf{n}_0$  and simple shear perpendicular to  $\mathbf{n}_0$ . In both cases, we see microstructure occurs over a finite deformation region, lowers the energy to a convex function, and eliminates discontinuities and unstable negative-gradient regions in the stress profile. Experiments with a range of uniaxial stretches (achieved by adhering at intermediate actuation temperatures) show a cross-hatch microstructure within the LCE which visibly coarsens and then vanishes as the relaxed state,  $\lambda_s$ , is approached (Fig. 3(a)). Cross-hatch microstructure evolution is also seen upon cooling of  $\lambda = 1$  samples under POM (SI [27] M4). An additional test case, perpendicular stretching in a thin sheet, is shown in Fig. S9, showing near-perfect agreement to the previous analytic results [16, 18]. Corresponding perpendicular stretching experiments (Fig. 2b) also show a long semi-soft plateau accompanied by visible stripes, consistent with material values  $\alpha \approx 0.05$ ,  $\lambda_s \approx 2$ , though with a markedly steeper stress post-plateau, which we attribute to finite extensibility.

Having tested the relaxed energy/stress functions, we minimize them to predict the instability. We consider an infinite slab of LCE, initially occupying  $-t < z < 0$ , that is clamped below, free above and has planar  $\mathbf{n}_0 = \hat{\mathbf{x}}$ . The final configuration is the minimum of the total energy  $W = \int W_N(\mathbf{\Lambda}) dV$  over permitted displacement fields  $\mathbf{u}$ . Recalling that  $\mathbf{\Lambda} = \mathbf{I} + \nabla \mathbf{u}$ , minimizing variationally requires stress balance,  $\partial_i P_{ji} = 0$ , with  $\mathbf{P}\hat{\mathbf{z}} = 0$  on top and  $P_{ji}$  being the  $ji$  component of  $\mathbf{P}$ . We first tackle this problem using finite elements. For numerical simplicity, we mimic incompressibility by taking  $W_N$  as a compressible but with a large bulk modulus of  $B = 100\mu$ :

$$W_N(\mathbf{\Lambda}) = W_{R2}(\mathbf{\Lambda}/\text{Det}\mathbf{\Lambda}^{1/3}) + \frac{1}{2}B(\text{Det}\mathbf{\Lambda} - 1)^2. \quad (5)$$

To minimize, we use a bespoke C code [23] that imposes periodicity in-plane, divides the slab into constant-

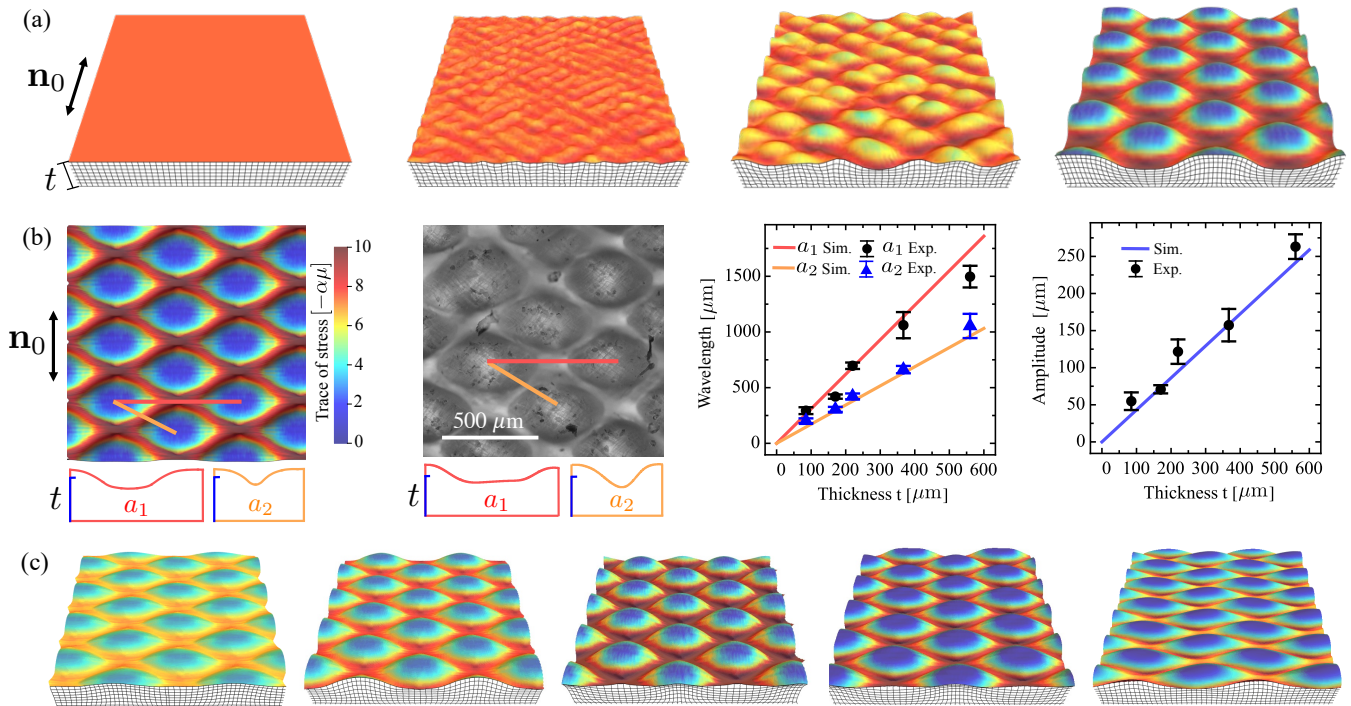


FIG. 4. (a) Dynamics and coarsening of the surface instability for  $(\lambda_s, \alpha) = (2, 0.05)$ . (b) Comparison of minimizing topographies, wavelengths and amplitudes between the simulation  $(\lambda_s, \alpha) = (2, 0.05)$  and the experiment ( $t = 220\mu\text{m}$ ). Wavelengths measured in POM, line profiles and amplitude from optical and scanning profilometry, errors are one standard deviation,  $n = 10$ . (c) Simulated equilibrium configurations for various  $(\lambda_s, \alpha)$ . From left to right:  $(\lambda_s, \alpha) = (1.44, 0.05)$ ,  $(1.71, 0.05)$ ,  $(2.15, 0.05)$ ,  $(2.15, 0.15)$ ,  $(2.15, 0.3)$ .

deformation tetrahedra, and moves nodes via damped Newtonian dynamics (see SI Sec. VII [27] for numerical details). An initial computation considers a near square slab with sides  $6.24t \times 6t$  and divided into 126k elements of characteristic size  $0.06t$ . The LCE is modeled with  $\lambda_s = 2$ ,  $\alpha = 0.05$ , and initialized at  $\mathbf{\Lambda} = \mathbf{I}$ . As seen in Fig. 4(a) and SI movie M5 [27], the free surface immediately destabilizes to oblique mesh-scale ripples, which coarsen via dynamics into an equilibrium cross-hatch strongly reminiscent of experiments. We then use fine-mesh simulations on a geometrically optimized unit cell with a range of values of  $\lambda_s$  and  $\alpha$  (i.e. different LCEs), to show that all are unstable, but with lower amplitude at lower  $\lambda_s$ , and shifting wave-vectors at higher  $\alpha$  (Fig. 4(c)). Equilibrium amplitude and wavelength are necessarily simply proportional to the problem's only length-scale,  $t$ , with values in good agreement with experiment. Moreover, in stark contrast to creasing, the topography is smooth and non-contacting.

Further insight is provided by linear stability analysis. Owing to finite compressibility, the equations of equilibrium admit a transitionally invariant base state  $\mathbf{\Lambda}_0 = \mathbf{I} + \gamma \hat{\mathbf{z}} \otimes \hat{\mathbf{z}}$ , where  $\gamma \sim \alpha\mu/B \sim 10^{-5}$  follows from the stress free top surface. Following Biot [20], we consider an infinite depth slab (half-space), and add small in-homogeneous displacement perturbations to the

base state,  $\mathbf{u} = \gamma z + \epsilon \mathbf{u}_1$ , resulting in a deformation  $\mathbf{\Lambda} = \mathbf{\Lambda}^0 + \epsilon \mathbf{\Lambda}^1$ . As we are perturbing about equilibrium the energy is only perturbed at quadratic order

$$W_N = W_N(\mathbf{\Lambda}^0) + \frac{1}{2} \epsilon^2 \left. \frac{\partial^2 W_N}{\partial \Lambda_{ij} \partial \Lambda_{lm}} \right|_{\mathbf{\Lambda}^0} \Lambda_{ij}^1 \Lambda_{lm}^1, \quad (6)$$

and, minimizing this variationally with respect to displacements gives the expected incremental stress-balance equations,  $\partial_i P_{ij}^1 = 0$  and  $\mathbf{P}^1 \mathbf{z} = 0$ , where  $P_{ij}^1 = \left. \frac{\partial^2 W_N}{\partial \Lambda_{ij} \partial \Lambda_{lm}} \right|_{\mathbf{\Lambda}^0} \Lambda_{lm}^1$ . Many of these energy derivatives are zero owing to the uniaxial material symmetry. The remainder, we evaluate numerically using finite differences, reducing the energy to a quadratic  $\nabla \mathbf{u}_1$ , and the stress-equations to homogeneous linear differential equations with constant coefficients. To find accurate derivatives, we explicitly re-compute the relaxed energy at the finite-difference test points. Interestingly, this careful evaluation reveals additional zero derivatives, corresponding to vanishing incremental moduli for shearing perpendicular to  $\mathbf{n}_0$ , as indicated by the energy plateau of  $W_{R2}$  in Fig. 3(b). Such vanishing moduli have been studied at the onset of monodomain director rotation [32, 33] but are here deep in the double laminate regime. The underlying cause is that the optimal micro-structure has four deformations with equal energy, and such shears are

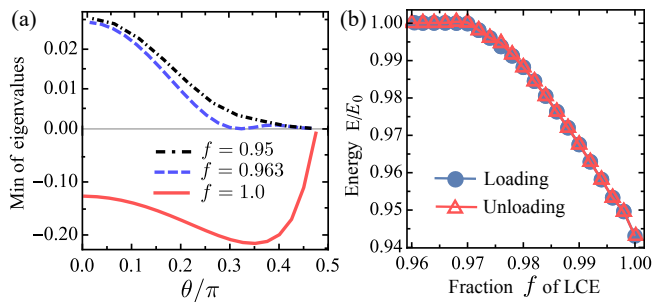


FIG. 5. (a) Minimal eigenvalue of Hessian against wave vector angle  $\theta$  for  $f = 0.95$  (stable),  $f = f_c = 0.963$  (instability threshold) and  $f = 1.0$  (pure LCE, unstable). The minimum eigenvalue for the  $f = 1$  case occurs at  $\theta_c \approx 0.35\pi$ , consistent with the numerical simulation ( $\theta_c \approx 0.355\pi$ ). (b) Loading ( $f$  increases) and unloading ( $f$  decreases) simulations confirm that the instability is super-critical with a threshold  $f_c \approx 0.97$ .  $E_0$  is the reference energy at the flat state.

accommodated simply by rearranging volume fractions. Similar vanishing curvatures are a common after convexification, e.g. in the 1D common-tangent construction.

To solve we substitute a trial solution that decays into the bulk,  $\mathbf{u}_1 = \exp(k\lambda z)\mathbf{v}(x, y)$ , and has undulates in plane with  $k$  vector along  $\mathbf{x}'$ , which makes an angle  $\theta$  with  $\mathbf{x}$  such that

$$\mathbf{v} = c_h \cos(kx')\hat{\mathbf{x}}' + c_g \cos(kx')\hat{\mathbf{y}}' + \sin(kx')\hat{\mathbf{z}}.$$

Substituting into the incremental stress equations (SI Sec. IX [27]) trigonometric, exponential and  $k$  factors cancel, leaving dimensionless algebraic equations for  $c_g$ ,  $c_h$  and  $\lambda$ . Explicitly solving for  $c_g(\lambda)$  and  $c_h(\lambda)$  reveals that the final condition is a quadratic in  $\lambda^2$ . Finally, solving and selecting only modes that decay with depth gives:

$$\mathbf{u}_1 = c_1 \exp(k\lambda_1 z)\mathbf{v}(\lambda_1) + c_2 \exp(k\lambda_2 z)\mathbf{v}(\lambda_2).$$

To assess stability, we substitute into the perturbed energy and integrate spatially, giving a quadratic  $c_1$  and  $c_2$ . Stability follows from the Hessian, with any negative eigenvalue revealing a growing perturbation that saves energy. As inevitable in a scale-free half-space, stability is independent of  $k$  which factors out of the integrated energy. More surprisingly, all wave-vector angles are unstable, despite the uni-axial symmetry. We thus assess the relative degree of instability from the magnitude of the negative eigenvalue, revealing an oblique perturbation will grow fastest (Fig. 5(a)), in agreement with experiment and simulation.

Since an isotropic LCE is simply neo-Hookean, we may approximate cooling via the energy  $(1 - f)W_{NH}(\mathbf{\Lambda}) + fW_{R2}(\mathbf{\Lambda})$ , and then vary  $f$  as a proxy for temperature. This allows us to explore onset, which, in both finite-elements and linear analysis is seen to occur at  $f \approx 0.96 - 0.97$  — i.e. almost pure LCE. Finite elements

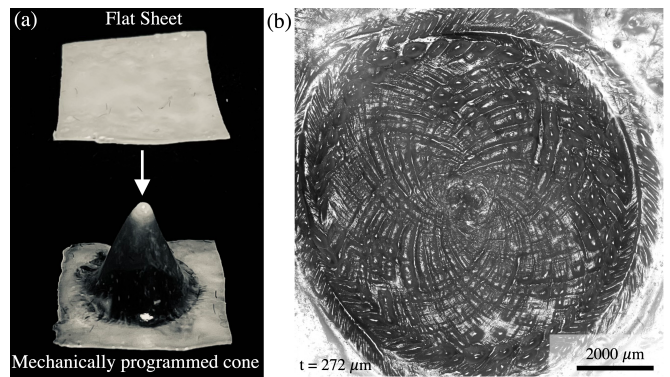


FIG. 6. (a) Photograph of an initially flat sheet mechanically programmed into a cone. (b) Micrograph of resulting surface instability at room temperature of a cone adhered to a surface in its flat state.

also show onset is super-critical, with topography appearing continuously and without hysteresis (Fig. 5(b)). This contrasts with sub-critical creasing, likely due to the lack of cusps.

Overall, our work thus highlights how the dramatically different constitutive law of LCEs still supports a compressive surface instability with similar scale-free properties to Biot creasing, but also with fundamental differences in pattern, criticality and singularity. Our work also provides a realistic constitutive law for microstructure forming nematic LCEs, which we believe justifies further study, and provides a basis of LCE mechanical engineering. We also highlight how pattern forming instabilities offer a different route to complex shape change in LCEs without patterned fabrication. Previous theoretical work on LCE instabilities [34], including ballooning [35, 36], cavitation [37], and wrinkling [38, 39], suggests this will be a rich theme for future research, potentially greatly enabled by the relaxed microstructural energies developed here. Naturally, one may also combine instabilities with simple pre-patterning to tailor the morphology. As an example, we repeat the experiment with a slab with approximately radial director imprinting (fabricated by forming a cone during mechanical programming), which generates the cross-hatch instability but in a striking log-spiral form (Fig. 6). Finally, we note that in all cases, the surface instability delivers high angle topography, suggesting applications in switchable aerodynamics, haptics, wettability and friction.

This work was supported by a UKRI ‘future leaders fellowship’ grant (grant no. MR/S017186/1).

\* jsb56@cam.ac.uk

- [1] M. Warner and E. M. Terentjev, *Liquid crystal elastomers*, Vol. 120 (Oxford university press, 2007).
- [2] J. Küpfer and H. Finkelmann, Nematic liquid single

- crystal elastomers, *Die Makromolekulare Chemie, Rapid Communications* **12**, 717 (1991).
- [3] P.-G. De Gennes, M. Hébert, and R. Kant, Artificial muscles based on nematic gels, in *Macromolecular Symposia*, Vol. 113 (Wiley Online Library, 1997) pp. 39–49.
- [4] T. J. White and D. J. Broer, Programmable and adaptive mechanics with liquid crystal polymer networks and elastomers, *Nature materials* **14**, 1087 (2015).
- [5] C. Modes, K. Bhattacharya, and M. Warner, Gaussian curvature from flat elastica sheets, *Proceedings of the Royal Society A: Mathematical, Physical and Engineering Sciences* **467**, 1121 (2011).
- [6] T. Guin, M. J. Settle, B. A. Kowalski, A. D. Auguste, R. V. Beblo, G. W. Reich, and T. J. White, Layered liquid crystal elastomer actuators, *Nature communications* **9**, 2531 (2018).
- [7] H. Aharoni, Y. Xia, X. Zhang, R. D. Kamien, and S. Yang, Universal inverse design of surfaces with thin nematic elastomer sheets, *Proceedings of the National Academy of Sciences* **115**, 7206 (2018).
- [8] M. Barnes and R. Verduzco, Direct shape programming of liquid crystal elastomers, *Soft Matter* **15**, 870 (2019).
- [9] J. A. Thomson, On growth and form (1917).
- [10] L. Golubović and T. Lubensky, Nonlinear elasticity of amorphous solids, *Physical review letters* **63**, 1082 (1989).
- [11] M. Warner, P. Bladon, and E. Terentjev, “soft elasticity”—deformation without resistance in liquid crystal elastomers, *Journal de Physique II* **4**, 93 (1994).
- [12] K. Urayama, S. Honda, and T. Takigawa, Deformation coupled to director rotation in swollen nematic elastomers under electric fields, *Macromolecules* **39**, 1943 (2006).
- [13] D. Corbett and M. Warner, Deformation and rotations of free nematic elastomers in response to electric fields, *Soft Matter* **5**, 1433 (2009).
- [14] K. Bhattacharya, *Microstructure of Martensite: Why it forms and how it gives rise to the shape-memory effect*, Vol. 2, Oxford Series on Materials Modelling (Oxford University Press, 2003).
- [15] G. Verwey, M. Warner, and E. Terentjev, Elastic instability and stripe domains in liquid crystalline elastomers, *Journal de Physique II* **6**, 1273 (1996).
- [16] H. Finkelmann, I. Kundler, E. Terentjev, and M. Warner, Critical stripe-domain instability of nematic elastomers, *Journal de Physique II* **7**, 1059 (1997).
- [17] A. DeSimone and G. Dolzmann, Macroscopic response of nematic elastomers via relaxation of a class of so (3) invariant energies, *Archive for rational mechanics and analysis* **161**, 181 (2002).
- [18] S. Conti, A. DeSimone, and G. Dolzmann, Semisoft elasticity and director reorientation in stretched sheets of nematic elastomers, *Physical Review E* **66**, 061710 (2002).
- [19] J. Biggins, Textured deformations in liquid crystal elastomers, *Liquid Crystals* **36**, 1139 (2009).
- [20] M. A. Biot, *Mechanics of incremental deformations* (1965).
- [21] V. Trujillo, J. Kim, and R. C. Hayward, Creasing instability of surface-attached hydrogels, *Soft Matter* **4**, 564 (2008).
- [22] E. Hohlfeld and L. Mahadevan, Unfolding the sulcus, *Physical review letters* **106**, 105702 (2011).
- [23] T. Tallinen, J. S. Biggins, and L. Mahadevan, Surface sulci in squeezed soft solids, *Physical review letters* **110**, 024302 (2013).
- [24] A. E. Shyer, T. Tallinen, N. L. Nerurkar, Z. Wei, E. S. Gil, D. L. Kaplan, C. J. Tabin, and L. Mahadevan, Villification: how the gut gets its villi, *Science* **342**, 212 (2013).
- [25] T. Tallinen, J. Y. Chung, J. S. Biggins, and L. Mahadevan, Gyrification from constrained cortical expansion, *Proceedings of the National Academy of Sciences* **111**, 12667 (2014).
- [26] G. Verwey and M. Warner, Compositional fluctuations and semisoftness in nematic elastomers, *Macromolecules* **30**, 4189 (1997).
- [27] See Supplemental Information for the supporting movies, experimental details, numerical methods, and theoretical analysis.
- [28] C. Yakacki, M. Saed, D. Nair, T. Gong, S. Reed, and C. Bowman, Tailorable and programmable liquid-crystalline elastomers using a two-stage thiol–acrylate reaction, *Rsc Advances* **5**, 18997 (2015).
- [29] P. Bladon, E. Terentjev, and M. Warner, Transitions and instabilities in liquid crystal elastomers, *Physical Review E* **47**, R3838 (1993).
- [30] S. A.J.M., *Deformations of Fibre-reinforced Materials* (Clarendon press, Oxford, 1972).
- [31] M. Destrade, B. M. Donald, J. Murphy, and G. Saccomandi, At least three invariants are necessary to model the mechanical response of incompressible, transversely isotropic materials, *Computational Mechanics* **52**, 959 (2013).
- [32] F. Ye, R. Mukhopadhyay, O. Stenull, and T. C. Lubensky, Semisoft nematic elastomers and nematics in crossed electric and magnetic fields, *Physical review letters* **98**, 147801 (2007).
- [33] J. Biggins, E. Terentjev, and M. Warner, Semisoft elastic response of nematic elastomers to complex deformations, *Physical Review E* **78**, 041704 (2008).
- [34] L. A. Mihai and A. Goriely, Instabilities in liquid crystal elastomers, *MRS Bulletin* **46**, 784 (2021).
- [35] A. Giudici and J. S. Biggins, Giant deformations and soft-inflation in Ice balloons, *Europhysics Letters* **132**, 36001 (2020).
- [36] V. Lee and K. Bhattacharya, Actuation of cylindrical nematic elastomer balloons, *Journal of Applied Physics* **129**, 114701 (2021).
- [37] V. Lee and K. Bhattacharya, Universal deformations of ideal liquid crystal elastomers, arXiv preprint arXiv:2210.17372 (2022).
- [38] M. S. Krieger and M. A. Dias, Tunable wrinkling of thin nematic liquid crystal elastomer sheets, *Physical Review E* **100**, 022701 (2019).
- [39] A. Goriely and L. A. Mihai, Liquid crystal elastomers wrinkling, *Nonlinearity* **34**, 5599 (2021).

# Supplemental Information: Surface instability in a nematic elastomer

Morgan Barnes,<sup>1</sup> Fan Feng,<sup>1</sup> and John S. Biggins<sup>1,\*</sup>

<sup>1</sup>*Department of Engineering, University of Cambridge,  
Trumpington St., Cambridge CB2 1PZ, United Kingdom*

(Dated: March 20, 2023)

## I. MATERIAL FABRICATION

### A. Materials

1,4-bis-[4-(3-acryloyloxypropyloxy)benzoyloxy]-2-methylbenzene (RM257) was purchased from Wilshire technologies. 2,20 -(Ethylenedioxy) diethanethiol (EDDET), pentaerythritol tetrakis (3-mercaptopropionate) (PETMP), chloroform, dipropyl amine (DPA), and (2-hydroxyethoxy)-2- methylpropiophenone (HHMP) were obtained from Sigma Aldrich. All materials were used as received.

### B. Synthesis

LCEs were synthesized as previously reported. [S1] RM257 (588 mg, 1 mmol), EDDET (124.09 mg, 0.6818 mmol), PETMP (55.45 mg, 0.1136 mmol), 0.5 wt% HHMP (3.84 mg), and 40 wt% chloroform (307 mg) were combined in a scintillation vial, heated to 80°C, and vortexed until all reagents were dissolved and mixed. Next, 0.23 mol% of DPA diluted to 2 wt% in chloroform (0.417 mg DPA in 20.44 mg chloroform) was added to the mixture to catalyze the thiol-acrylate Michael addition. The mixture was deposited between two glass slides separated by spacers of desired thickness. After 2 hours the LCE film was removed from the glass cell and heated to 100°C for 1 hour to evaporate the remaining chloroform, resulting in an opaque polydomain LCE. For monodomain alignment, the LCE was stretched to double its length and UV cured for 10 minutes to crosslink the excess acrylates. The resulting spontaneous actuation,  $\lambda_s$  is shown in Figure S2. For a cone LCE, the polydomain LCE was clamped to metal sheet with a circular cutout of the desired cone diameter. A toothpick was then inserted into the center of the circle to produce a cone, the toothpick was removed to allow the cone to relax to  $\lambda \approx 2$  and then UV cured.

### C. Surface Instabilities

Surface instabilities for strains  $= \lambda_s$  were achieved by heating programmed LCEs to their fully actuated (isotropic) flat state (130°C) and quickly pressing a glass slide coated with brush-on Loctite super glue onto the LCE. After adhered the LCE is cooled to room temperature to produce the surface instabilities (Figs. 1(b), 4(b), 6, S4)

### D. Crosshatch Microstructure

To achieve cross-hatch microstructures for strains less than  $\lambda_s$ , (as shown in Fig. 3) the LCEs were uniformly heated to temperatures less than 130°C to achieve partial contraction, adhered onto a glass slide, and cooled to room temperature.

---

\* jsb56@cam.ac.uk

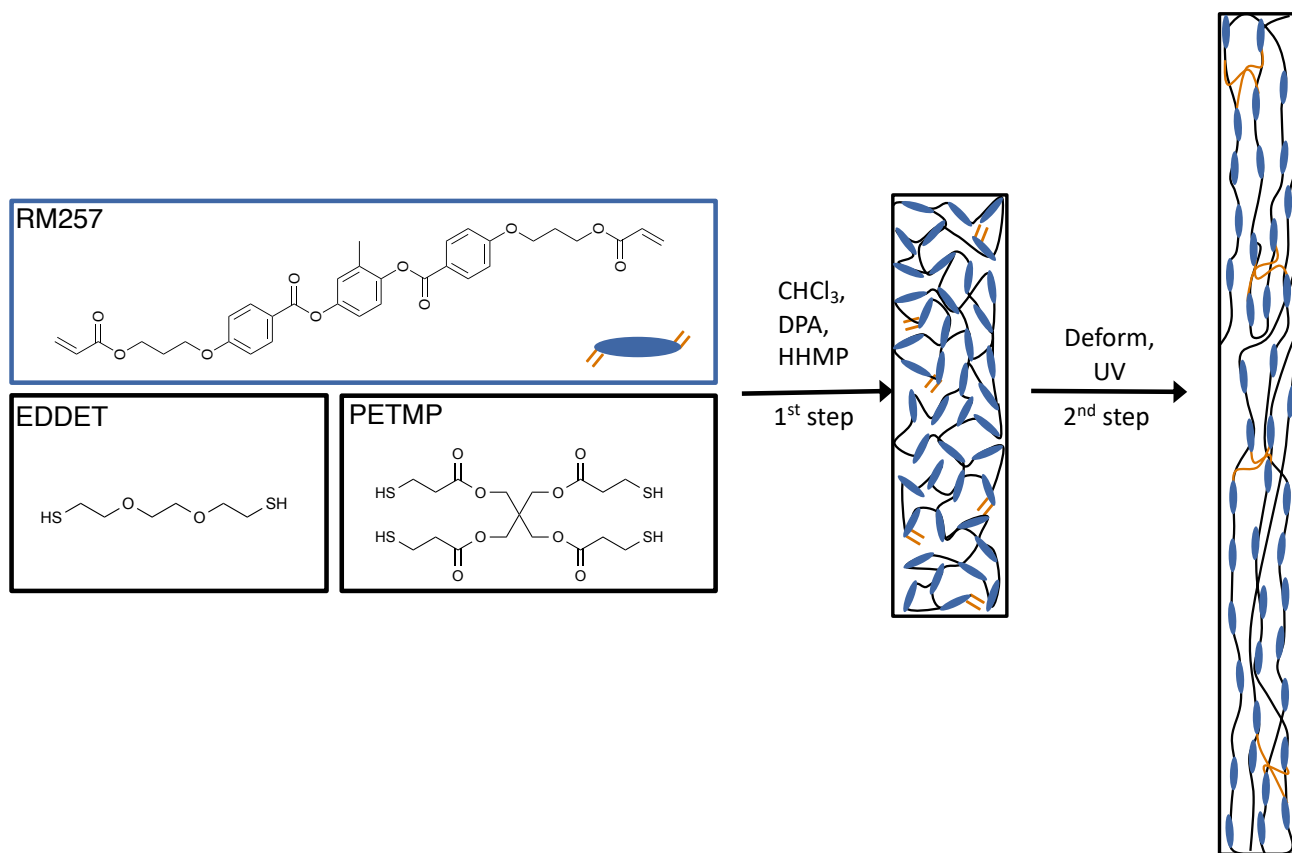


FIG. S1. Schematic of LCE chemistry and two-step synthesis.

## II. GENERAL CHARACTERIZATION

### A. Tensile Testing

Tensile data was acquired using an Instron 5584 equipped with a 10 N load cell. An LCE (10 mm X 0.23 mm X 30 mm) was stretched perpendicularly to the programmed director at a pulling speed of 0.0009 % strain/second.

### B. Polarized Optical Microscopy

Cross-polarized optical micrographs were taken using a Nikon Eclipse LV100nd microscope in transmission mode.

### C. Actuation

Actuation vs. temperature (Fig. S2) data was acquired by measuring the distance between points of a monodomain LCE while heating the LCE using a Linkham LTS420 hot stage from room temperature to 150°C with a temperature step of 5°C and allowing the LCE to equilibrate for 5 minutes after each step.

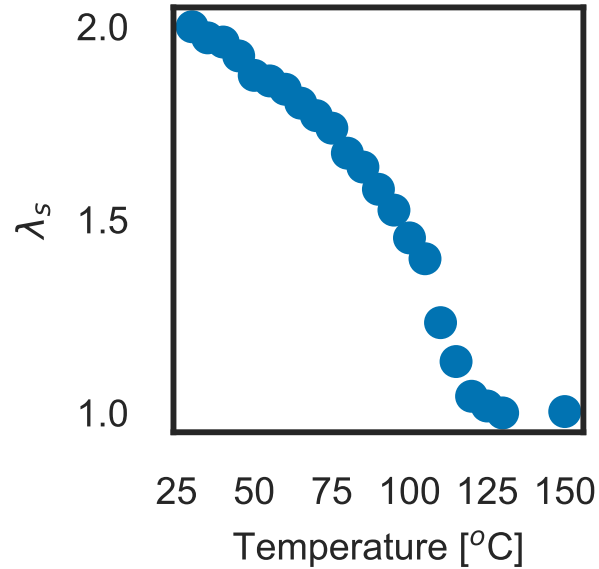


FIG. S2. Spontaneous actuation of a monodomain LCE in response to temperature.

### III. SURFACE INSTABILITY CHARACTERIZATION

#### A. Optical Profilometry

Depth topography images were obtained with an Olympus BX51 optical microscope. Montage images (Fig. S5) and height maps (Fig. S6) were created within the Olympus LAS software by merging the z-stack images to calculate the optimum focal depth for each pixel on the surface. Wavelength measurements were calculated by manually calculating the periodic distance between surface features in the montage images. Amplitude measurements were calculated by extracting the local minimum and maximum for each surface feature period.

Large length scale images (Figs. S3, S4) were captured using the stitching feature on the LAS software with 20% overlap.

#### B. Scanning Profilometry

Height line scans (Fig. S7(a)) were collected using a Taylor Hobson Talysurf 120 profilometer and scanned parallel to the nematic director. Surface depth contour plots were created by stacking multiple line scans (Fig. S7(b)) and amplitudes of the surface features were calculated by extracting the local minimum and maximum for each surface feature period.

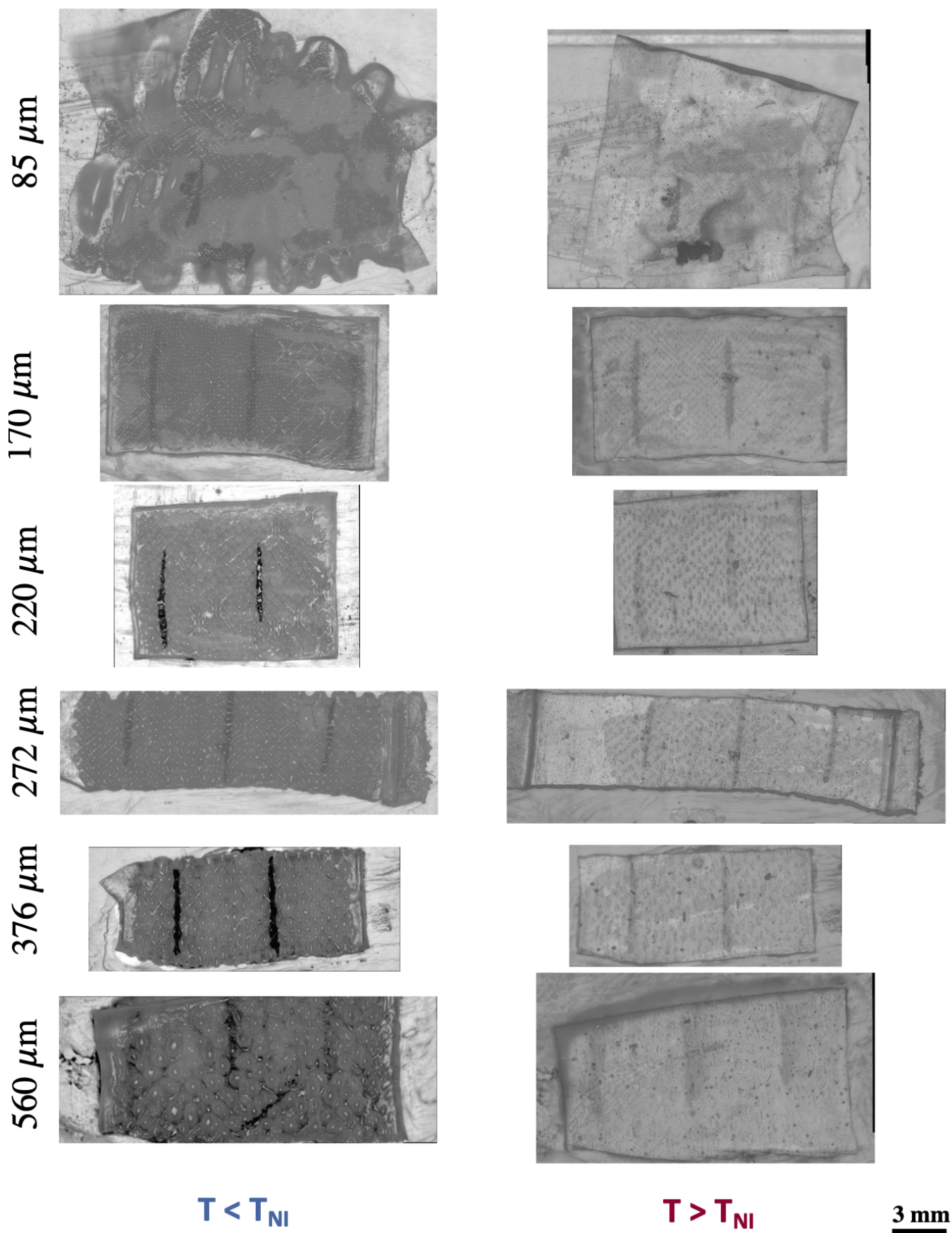


FIG. S3. Micrographs of surface instability for monodomain LCEs with varying thicknesses when hot ( $130^\circ\text{C}$ ) and cold (room temperature). Heated LCEs show some optical artifacts of surface instability but the surface is smooth as shown in the heated depth topography as shown in Fig. 1(b).

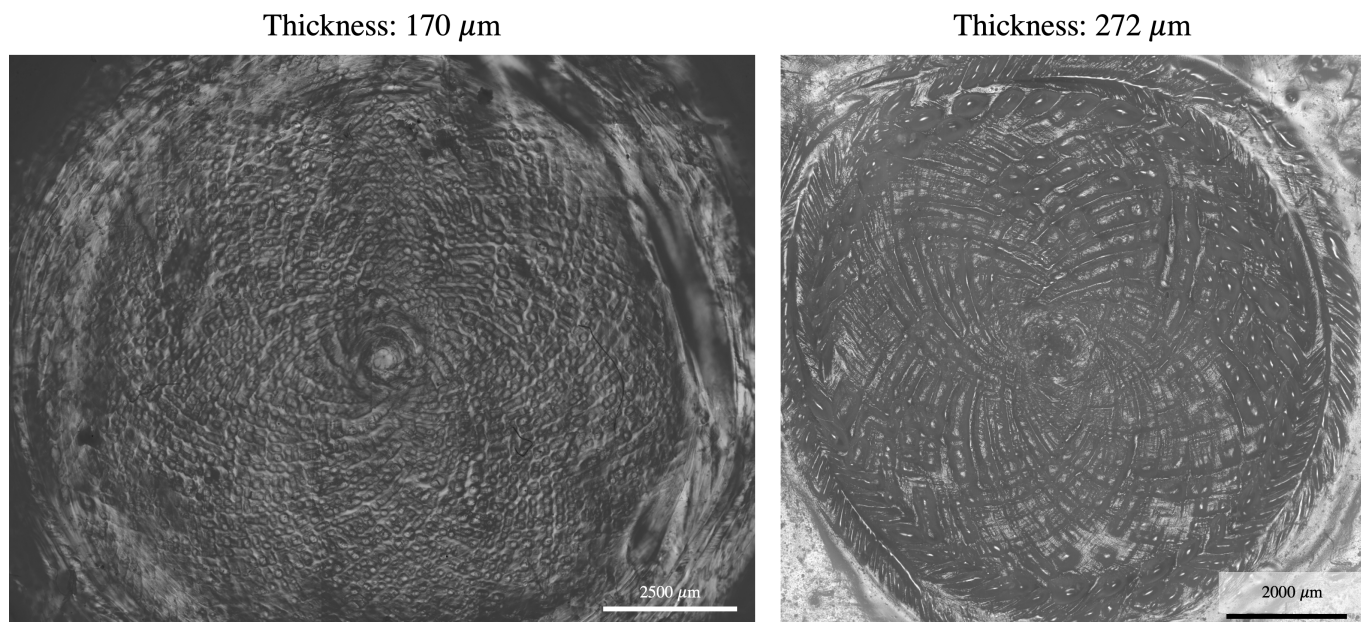


FIG. S4. Micrographs of the surface instability of LCE cones adhered to glass at  $T = 130^\circ\text{C}$ .

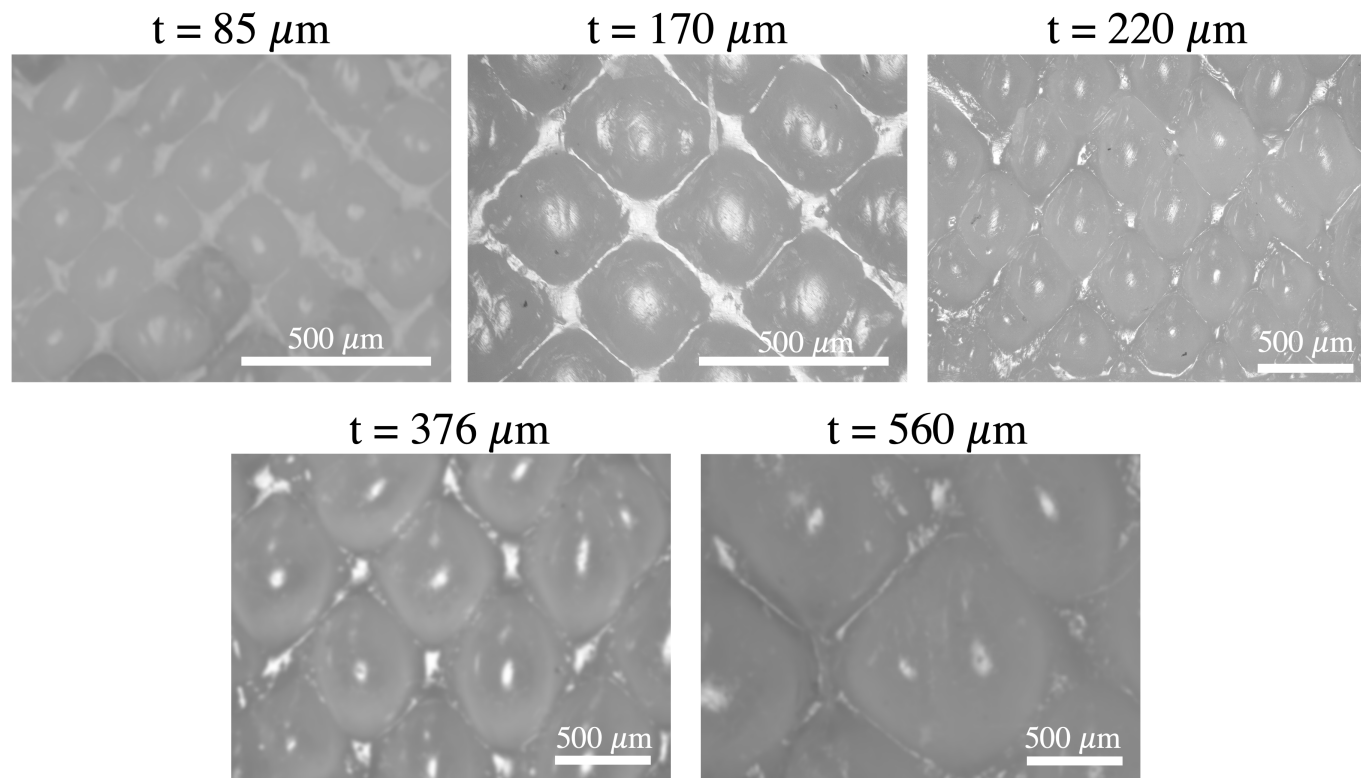


FIG. S5. Micrographs of surface instability of monodomain LCEs with  $\lambda_s = 2$  and glued down at the fully contracted ( $\lambda=1$ ) state at varying thicknesses.

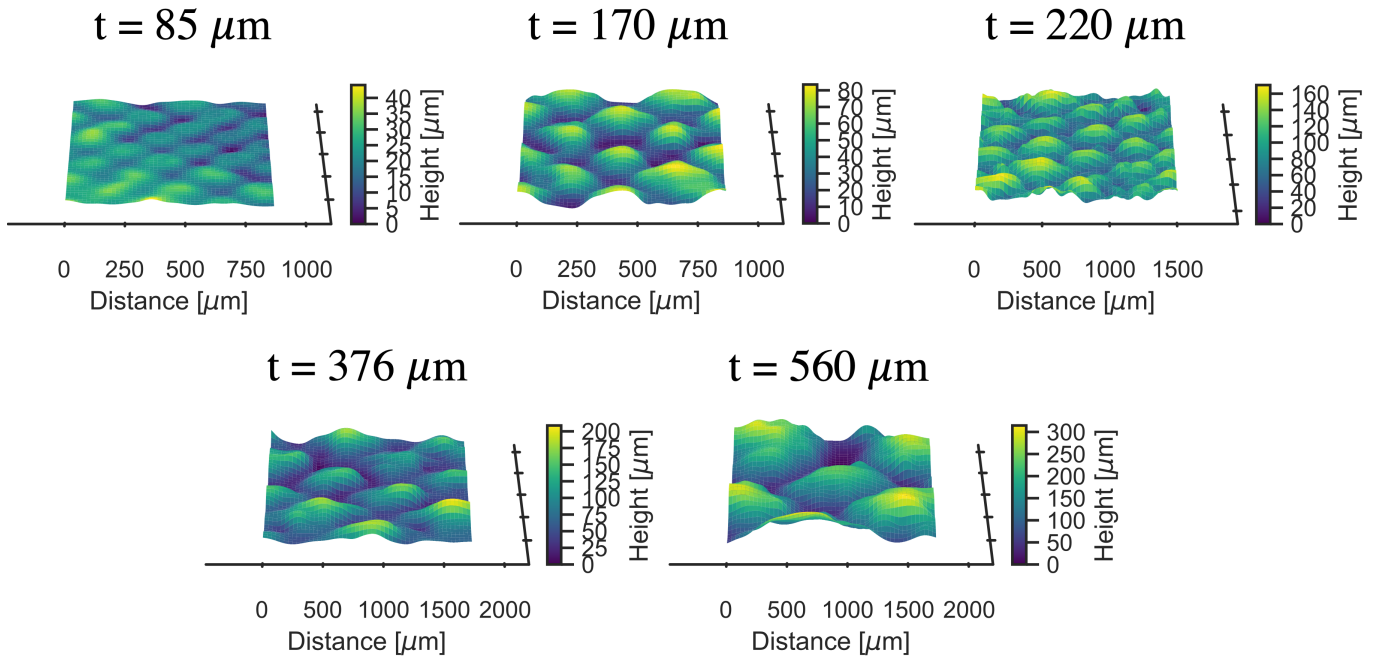


FIG. S6. Depth topography of the surface instability of monodomain LCEs with  $\lambda_s = 2$  and glued down at the fully contracted ( $\lambda=1$ ) state at varying thickness.

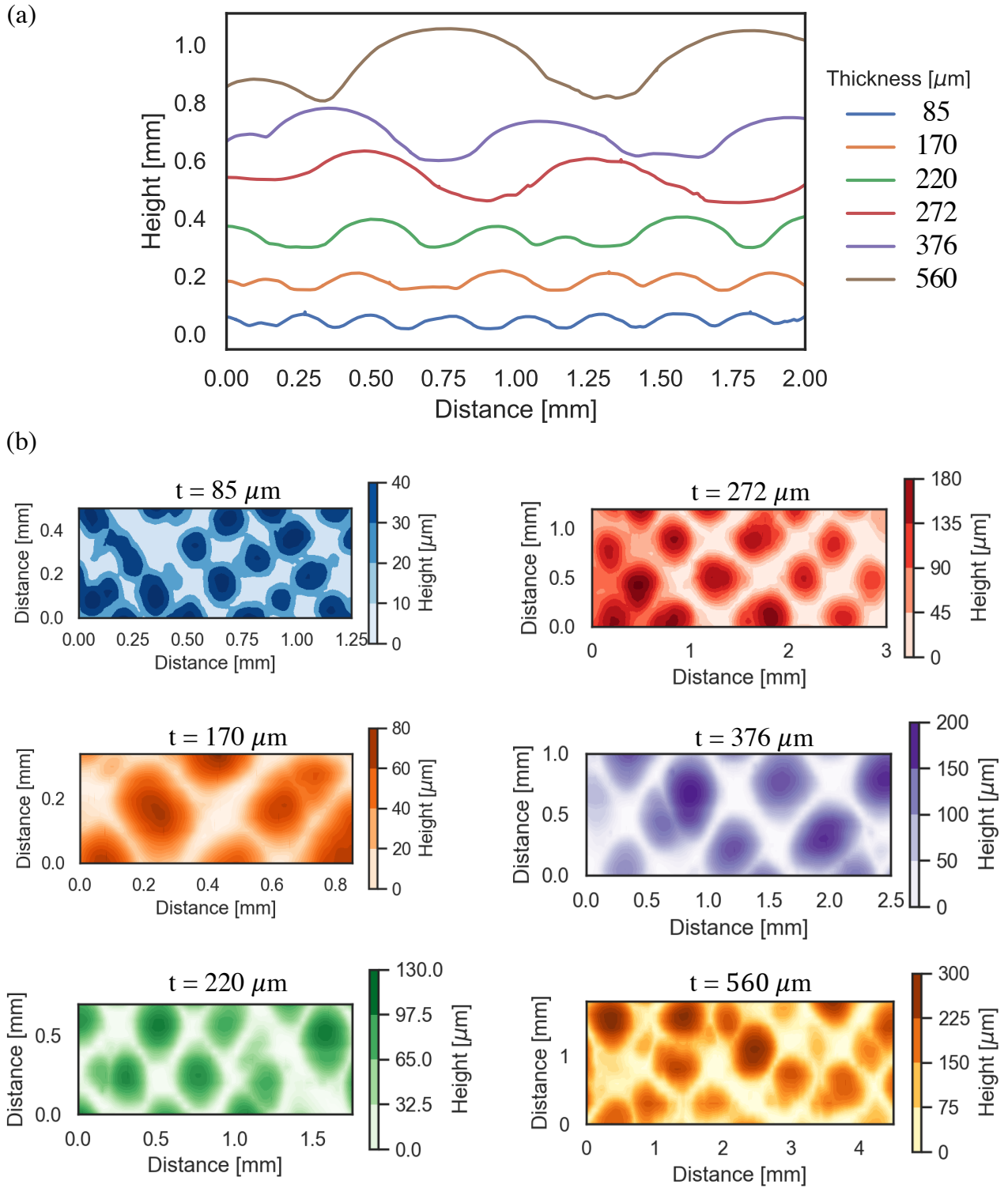


FIG. S7. (a) Representative line scans (with vertical line shifts for viewability) of surface topography of monodomain LCEs with  $\lambda_s = 2$  and glued down at the fully contracted ( $\lambda=1$ ) state at varying thickness. (b) Constructed height contour maps created from a series of line scans.

#### IV. IDEAL AND NON-IDEAL LCE ENERGY

Upon cooling, an LCE slab in the isotropic state can transform to the nematic state via a spontaneous deformation gradient  $\mathbf{\Lambda}_s(\mathbf{n}) = \lambda_s \mathbf{n} \otimes \mathbf{n} + \lambda_s^{-1/2}(\mathbf{I} - \mathbf{n} \otimes \mathbf{n})$ . If the subsequent deformation follows the neo-Hookean constitutive law, the ideal LCE energy may be given by  $W_{NH}(\mathbf{\Lambda}\mathbf{\Lambda}_s^{-1}(\mathbf{n}))$ , where  $\mathbf{\Lambda}$  is the deformation gradient from the isotropic state to the nematic state and  $W_{NH}$  is the neo-Hookean energy density given by  $W_{NH}(\mathbf{\Lambda}) = \frac{1}{2}\mu \text{Tr}(\mathbf{\Lambda}\mathbf{\Lambda}^T)$ . Allowing the director  $\mathbf{n}$  to rotate arbitrarily without any energy cost, we obtain an ideal energy solely depending on  $\mathbf{\Lambda}$ :

$$W_I(\mathbf{\Lambda}) = \min_{\mathbf{n}} W_{NH}(\mathbf{\Lambda}\mathbf{\Lambda}_s^{-1}) = \frac{1}{2}(\Lambda_1^2\lambda_s + \Lambda_2^2\lambda_2 + \Lambda_3^2/\lambda_s^2), \quad (\text{S1})$$

where  $\Lambda_1 \leq \Lambda_2 \leq \Lambda_3$  are ordered principal stretches of  $\mathbf{\Lambda}$ . However, owing to the fabrication, the rotation of  $\mathbf{n}$  may cost a small amount of energy characterized by a small non-ideality factor  $\alpha$ , leading to the non-ideal energy:

$$W_{NI}(\mathbf{\Lambda}) = \min_{\mathbf{n}} \left( W_{NH}(\mathbf{\Lambda}\mathbf{\Lambda}_s^{-1}(\mathbf{n})) + \frac{1}{2}\alpha\lambda_s\mu \text{Tr}(\mathbf{\Lambda}(\mathbf{I} - \mathbf{n}_0 \otimes \mathbf{n}_0)\mathbf{\Lambda}^T \mathbf{n} \otimes \mathbf{n}) \right). \quad (\text{S2})$$

To minimize over  $\mathbf{n}$ , we collect all terms containing  $\mathbf{n}$  and rewrite  $W_{NI}(\mathbf{\Lambda})$  as

$$W_{NI}(\mathbf{\Lambda}) = \min_{\mathbf{n}} \left( \frac{1}{2}\lambda_s\mu \text{Tr}(\mathbf{\Lambda}\mathbf{\Lambda}^T + \mathbf{M}\mathbf{n} \otimes \mathbf{n}) \right), \quad (\text{S3})$$

where  $\mathbf{M} = (\lambda_s^{-3} - 1)\mathbf{\Lambda}\mathbf{\Lambda}^T + \alpha\mathbf{\Lambda}(\mathbf{I} - \mathbf{n}_0 \otimes \mathbf{n}_0)\mathbf{\Lambda}^T$ . In the admissible domain of  $\lambda_s \sim 1.2 - 2.5$  and  $\alpha \sim 0.05 - 0.3$ ,  $\mathbf{M}$  is negative definite, and thus the minimizer  $\mathbf{n}$  lies along the eigenvector corresponding to the smallest negative eigenvalue of  $\mathbf{M}$ . Specifically, let the corresponding eigenvalues and eigenvectors of  $\mathbf{M}$  be  $m_i$  and  $\mathbf{u}_i$  for  $i = 1, 2, 3$ , and  $m_1 \leq m_2 \leq m_3 < 0$ . Then  $W_{NI}(\mathbf{\Lambda})$ , after minimizing over  $\mathbf{n}$  for a fixed  $\mathbf{n}_0$ , may be written as

$$W_{NI}(\mathbf{\Lambda}) = \frac{1}{2}\lambda_s\mu (\text{Tr}(\mathbf{\Lambda}\mathbf{\Lambda}^T) + m_1). \quad (\text{S4})$$

Next, we compute the first Piola–Kirchhoff (PK1) stress  $\mathbf{P}_{NI}$  by differentiating the non-ideal energy  $W_{NI}(\mathbf{\Lambda}J^{-1/3})$  directly in the slightly compressible regime ( $J = \text{Det}\mathbf{\Lambda} \approx 1$ ). Notice that  $m_1$  is also a function of  $\mathbf{\Lambda}$ . Thus the PK1 stress includes the contribution of  $m_1$  and is given by

$$\mathbf{P}_{NI}(\mathbf{\Lambda}) = \frac{\partial W_{NI}(\mathbf{\Lambda}J^{-1/3})}{\partial \mathbf{\Lambda}} = \mu\lambda_s J^{-2/3} \left( \mathbf{\Lambda} + m_1\mathbf{u}_1 \otimes \mathbf{\Lambda}^{-1}\mathbf{u}_1 - \frac{1}{3}(\text{Tr}(\mathbf{\Lambda}\mathbf{\Lambda}^T) + m_1)\mathbf{\Lambda}^{-T} \right). \quad (\text{S5})$$

Accordingly, the Cauchy stress  $\boldsymbol{\sigma}_{NI}(\mathbf{\Lambda})$  is expressed as

$$\boldsymbol{\sigma}_{NI}(\mathbf{\Lambda}) = J^{-1}\mathbf{P}_{NI}(\mathbf{\Lambda})\mathbf{\Lambda}^T = \mu\lambda_s J^{-5/3} \left( \mathbf{\Lambda}\mathbf{\Lambda}^T + m_1\mathbf{u}_1 \otimes \mathbf{u}_1 - \frac{1}{3}(\text{Tr}(\mathbf{\Lambda}\mathbf{\Lambda}^T) + m_1)\mathbf{I} \right). \quad (\text{S6})$$

**Remark 1.** The non-ideal energy  $W_{NI}(\mathbf{\Lambda})$  is transversely isotropic, i.e.,  $W_{NI}(\mathbf{\Lambda}) = W_{NI}(\mathbf{R}\mathbf{\Lambda}\mathbf{R}\mathbf{n}_0)$  with  $\mathbf{R}$  being an arbitrary rotation and  $\mathbf{R}\mathbf{n}_0$  a rotation about  $\mathbf{n}_0$ .

**Remark 2.** The ideal energy  $W_{NI}(\mathbf{\Lambda})$  in this paper is related to the ‘‘trace formula’’ by  $\lambda_s = r^{1/3}$ . The latter is directly derived from statistical mechanics [S2]. If the deformation gradient is with respect to a reference state being stretched from the isotropic state, the non-ideal energy may be written in a different form. For example, the deformation gradient  $\tilde{\mathbf{\Lambda}}$  in [S3] is related to  $\mathbf{\Lambda}$  by  $\mathbf{\Lambda} = \tilde{\mathbf{\Lambda}}b^{-1/6}(\mathbf{I} + (b^{1/2} - 1)\mathbf{n}_0 \otimes \mathbf{n}_0)$  with  $b = 1 + \alpha\lambda_s^3/(1 - \lambda_s^3)$ . Accordingly, the non-ideal energy may be rewritten as a compact form:

$$W_{NI}(\tilde{\mathbf{\Lambda}}) = (\text{Det}\tilde{\mathbf{\Lambda}})^2 - \tilde{\alpha}|\tilde{\mathbf{\Lambda}}^T\mathbf{n}|^2 - \tilde{\beta}|\tilde{\mathbf{\Lambda}}\mathbf{n}_0|^2, \quad (\text{S7})$$

where  $\tilde{\alpha} = 1 - \alpha - \lambda_s^{-3}$  and  $\tilde{\beta} = -\alpha\lambda_s^3/(1 - \lambda_s^3)$ .

#### V. RELAXATION OF THE NON-IDEAL LCE ENERGY

By forming compatible laminates, the ideal and non-ideal energies are convexified to relaxed energies. As a result, the LCEs exhibit soft and semi-soft mechanical responses. The relaxed ideal energy in 3D and the relaxed non-ideal

energy in 2D have been studied [S3, S4]. However, the study of relaxed non-ideal energy in 3D is largely absent, hindering the understanding of 3D mechanical behavior, including surface instability in this work.

Here we compute the relaxed non-ideal energy in 3D numerically and use it to construct a new constitutive relation for the study of surface instability. To this end, we firstly compute the relaxed energy  $W_{R1}(\mathbf{\Lambda})$  by forming first-order laminates. A general shear is defined as  $\mathbf{S}(\boldsymbol{\gamma}, \hat{\mathbf{m}}) = \mathbf{I} + \boldsymbol{\gamma} \otimes \hat{\mathbf{m}}$  with  $\hat{\mathbf{m}}$  being the normal to the shear plane.  $\boldsymbol{\gamma}$  is perpendicular to  $\hat{\mathbf{m}}$  and encodes both the shear direction and amplitude. As shown in Fig. S8, a deformation gradient  $\mathbf{\Lambda}$  may be approximated by averaging two rank-1 deformation gradients  $\mathbf{\Lambda}_1$  and  $\mathbf{\Lambda}_2$  as

$$\mathbf{\Lambda} = f\mathbf{\Lambda}_1 + (1-f)\mathbf{\Lambda}_2, \quad (\text{S8})$$

where  $\mathbf{\Lambda}_1 = \mathbf{S}((1-f)\mathbf{a}, \hat{\mathbf{m}})\mathbf{\Lambda}$  and  $\mathbf{\Lambda}_2 = \mathbf{S}(-f\mathbf{a}, \hat{\mathbf{m}})\mathbf{\Lambda}$ . Then the relaxed energy  $W_{R1}(\mathbf{\Lambda})$  by minimizing over laminates is given by

$$W_{R1}(\mathbf{\Lambda}) = \min_{f, \hat{\mathbf{m}}, \mathbf{a} \perp \hat{\mathbf{m}}} (fW_{NI}(\mathbf{\Lambda}_1) + (1-f)W_{NI}(\mathbf{\Lambda}_2)). \quad (\text{S9})$$

Following the same procedure, we construct  $W_{R2}(\mathbf{\Lambda})$  by forming second-order twins:

$$W_{R2}(\mathbf{\Lambda}) = \min_{f, \hat{\mathbf{m}}, \mathbf{a} \perp \hat{\mathbf{m}}} (fW_{R1}(\mathbf{\Lambda}_1) + (1-f)W_{R1}(\mathbf{\Lambda}_2)), \quad (\text{S10})$$

replacing  $W_{NI}(\mathbf{\Lambda})$  in (S9) by  $W_{R1}(\mathbf{\Lambda})$ . Practically in the numerical minimization, we write  $\hat{\mathbf{m}}$  in terms of its Euler

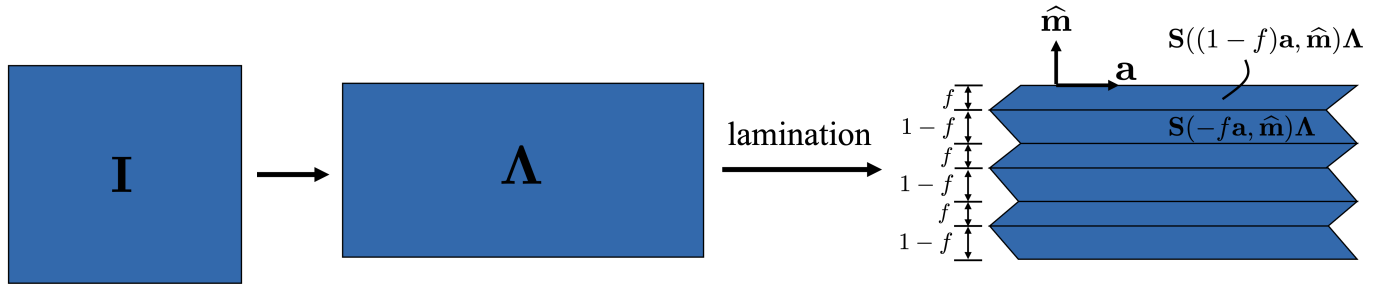


FIG. S8. Approximating the deformation gradient  $\mathbf{\Lambda}$  with first-order twin.

angles as

$$\hat{\mathbf{m}} = (\cos n_\theta, \sin n_\theta \cos n_\phi, \sin n_\theta \sin n_\phi), \quad (\text{S11})$$

and  $\mathbf{a} = s\hat{\mathbf{a}}$  with magnitude  $s$  and direction

$$\hat{\mathbf{a}} = \cos m_\phi(0, -\sin n_\phi, \cos n_\phi) + \sin m_\phi(-\sin n_\phi, \cos n_\theta \cos n_\phi, \cos n_\theta \sin n_\phi). \quad (\text{S12})$$

Then we may perform the minimizations (S9) and (S10) over the generalized vector  $\boldsymbol{\ell} = (f, n_\theta, n_\phi, m_\phi, s)$  in the domain  $\mathcal{D} = [0, 1] \times [0, \pi] \times [0, 2\pi] \times [0, 2\pi] \times \mathbb{R}$ . Here the amplitude of shear  $s$  is restricted in a finite range for a sensible result, making  $\mathcal{D}$  a finite domain.

To discretize the domain of  $\mathbf{\Lambda}$ , we notice that  $W_{R1}(\mathbf{\Lambda})$  is invariant under any rotation about  $\mathbf{n}_0$ . Obeying incompressibility and frame indifference, we may represent  $\mathbf{\Lambda}$  by any four independent scalar invariants. Herein, we use  $(\Lambda_1, \Lambda_3, \theta, \phi)$ , with  $\Lambda_1 \leq \lambda_2 \leq \Lambda_3$  being the three eigenvalues of  $\sqrt{\mathbf{\Lambda}^T \mathbf{\Lambda}}$ ,  $\theta$  the angle between  $\mathbf{n}_0$  and the plane spanned by corresponding eigenvectors  $\mathbf{u}_1$  and  $\mathbf{u}_3$ , and  $\phi$  the angle between  $\mathbf{u}_1$  and the projected vector of  $\mathbf{n}_0$  on that plane. If  $\theta = \pi/2$ , we define  $\phi = 0$ . Owing to the  $\mathbf{u}_i \rightarrow -\mathbf{u}_i$  invariance, we may restrict  $\theta$  and  $\phi$  in  $[0, \pi/2]$ . Finally, we discretize the 4D space  $(\Lambda_1, \Lambda_3, \theta, \phi) \in [0, 1] \times [1, 4] \times [0, \pi/2] \times [0, \pi/2]$  using  $11 \times 31 \times 11 \times 11 = 41261$  nodes. For each node, we construct a test deformation gradient  $\mathbf{\Lambda}_t(\Lambda_1, \Lambda_3, \theta, \phi)$  and then perform the minimization for  $\mathbf{\Lambda}_t$ .

The detailed numerical method is as follows. At each grid point  $(\Lambda_1, \Lambda_3, \theta, \phi)$ , we construct a test deformation gradient by

$$\mathbf{\Lambda}_t(\Lambda_1, \Lambda_3, \theta, \phi) = \Lambda_1 \mathbf{u}_1 \otimes \mathbf{u}_1 + \frac{1}{\Lambda_1 \Lambda_3} \mathbf{u}_2 \otimes \mathbf{u}_2 + \Lambda_3 \mathbf{u}_3 \otimes \mathbf{u}_3, \quad (\text{S13})$$

$$\text{where } \mathbf{u}_1 = (\cos \theta \cos \phi, -\sin \phi, \sin \theta \cos \phi),$$

$$\mathbf{u}_2 = (-\sin \theta, 0, \cos \theta),$$

$$\mathbf{u}_3 = (-\cos \theta \sin \phi, -\cos \phi, -\sin \theta \sin \phi).$$

We then perform the minimization S9 numerically in Mathematica, using a sequence of steps to ensure accurate answers throughout the domain, including areas where the homogeneous deformation is itself a local minimum.

1. Minimize at each grid point using `NMinimize` with the `SimulatedAnnealing` method, a global minimization in the finite 5D domain  $\mathcal{D}$ , returning a minimized energy  $W_{R1}(\mathbf{\Lambda})$  and its corresponding argument  $\ell = (f, n_\theta, n_\phi, m_\phi, s)$ , which is then saved as the current best microstructure at each grid point.
2. Minimize at each grid point using `FindMinimum` with `ConjugateGradient` method. This is a local minimization from a starting guess, and descends by evaluating the local gradient. At each grid point we take as initial guesses the result from step (1), and also 30 other starting points distributed over  $\mathcal{D}$ . The saved microstructure/energy at each point is updated to the lowest of these results.
3. `FindMinimum` at each grid point, using as starting points the current current best microstructure parameters at the eight adjacent grid points. If the best result obtained is lower than the saved microstructure, it is updated. This step allows optimal microstructures to propagate across the grid, and is repeated until convergence is achieved over the entire grid.

We find that the `ConjugateGradient` steps give very strong convergence to local minima if we provide analytic forms for the gradient  $\frac{\partial W_{R1}(\mathbf{\Lambda}_t)}{\partial \ell}$  which, for completeness, are displayed below:

$$\begin{aligned}
\frac{\partial W_{R1}(\mathbf{\Lambda}_t)}{\partial f} &= W_{NI}(\mathbf{\Lambda}_1) - W_{NI}(\mathbf{\Lambda}_2) - f \mathbf{a} \cdot \boldsymbol{\sigma}_{NI}(\mathbf{\Lambda}_1) \hat{\mathbf{m}} - (1-f) \mathbf{a} \cdot \boldsymbol{\sigma}_{NI}(\mathbf{\Lambda}_2) \hat{\mathbf{m}} \\
\frac{\partial W_{R1}(\mathbf{\Lambda}_t)}{\partial n_\theta} &= f(1-f) \mathbf{a} \cdot (\mathbf{P}_{NI}(\mathbf{\Lambda}_1) - \mathbf{P}_{NI}(\mathbf{\Lambda}_2)) \boldsymbol{\Lambda}_t^T \frac{\partial \hat{\mathbf{m}}}{\partial n_\theta} + f(1-f) (\boldsymbol{\sigma}_{NI}(\mathbf{\Lambda}_1) - \boldsymbol{\sigma}_{NI}(\mathbf{\Lambda}_2)) \hat{\mathbf{m}} \cdot \frac{\partial \mathbf{a}}{\partial n_\theta} \\
\frac{\partial W_{R1}(\mathbf{\Lambda}_t)}{\partial n_\phi} &= f(1-f) \mathbf{a} \cdot (\mathbf{P}_{NI}(\mathbf{\Lambda}_1) - \mathbf{P}_{NI}(\mathbf{\Lambda}_2)) \boldsymbol{\Lambda}_t^T \frac{\partial \hat{\mathbf{m}}}{\partial n_\phi} + f(1-f) (\boldsymbol{\sigma}_{NI}(\mathbf{\Lambda}_1) - \boldsymbol{\sigma}_{NI}(\mathbf{\Lambda}_2)) \hat{\mathbf{m}} \cdot \frac{\partial \mathbf{a}}{\partial n_\phi} \\
\frac{\partial W_{R1}(\mathbf{\Lambda}_t)}{\partial m_\phi} &= f(1-f) (\boldsymbol{\sigma}_{NI}(\mathbf{\Lambda}_1) - \boldsymbol{\sigma}_{NI}(\mathbf{\Lambda}_2)) \hat{\mathbf{m}} \cdot \frac{\partial \mathbf{a}}{\partial m_\phi} \\
\frac{\partial W_{R1}(\mathbf{\Lambda}_t)}{\partial s} &= f(1-f) (\boldsymbol{\sigma}_{NI}(\mathbf{\Lambda}_1) - \boldsymbol{\sigma}_{NI}(\mathbf{\Lambda}_2)) \hat{\mathbf{m}} \cdot \hat{\mathbf{a}}
\end{aligned} \tag{S14}$$

The resulting grid of energies  $W_{R1}(\Lambda_1, \Lambda_3, \theta, \phi)$  and microstructures  $\ell_1(\Lambda_1, \Lambda_3, \theta, \phi)$  are interpolated at cubic order in `Mathematica`, resulting in interpolated functions  $f_{W_{R1}}(\Lambda_1, \Lambda_3, \theta, \phi)$  and  $f_{\ell_1}(\Lambda_1, \Lambda_3, \theta, \phi)$ . A numerical approximation for any deformation gradient  $\tilde{\mathbf{\Lambda}}$ , is then given by first calculating the four parameters  $(\tilde{\Lambda}_1, \tilde{\Lambda}_3, \tilde{\theta}, \tilde{\phi})$  for  $\tilde{\mathbf{\Lambda}}$  and then evaluating the function  $f_{W_{R1}}$  to obtain its energy  $W_{R1}(\tilde{\mathbf{\Lambda}}) = f_{W_{R1}}(\tilde{\Lambda}_1, \tilde{\Lambda}_3, \tilde{\theta}, \tilde{\phi})$ , and similar for microstructure parameters  $\ell_1(\tilde{\mathbf{\Lambda}})$ .

The computation of  $W_{R2}(\mathbf{\Lambda}_t)$  then follows the same procedure as above, except replacing  $W_{NI}$  by the numerical  $W_{R1}(\mathbf{\Lambda})$ , and using numerical derivatives of  $W_{R1}(\mathbf{\Lambda})$  during `ConjugateGradient`. The result is again a grid of energies  $W_{R2}(\Lambda_1, \Lambda_3, \theta, \phi)$  and microstructures  $\ell_2(\Lambda_1, \Lambda_3, \theta, \phi)$ .

The lack of analytic derivatives, combined with numerical inaccuracies in  $W_{R1}(\mathbf{\Lambda})$ , mean that the R2 microstructures thus obtained are often unsatisfactorily converged into local minima, particularly for the subsequent estimation of stresses which relies on strong local convergence (see next section). We thus then perform, at each grid point, an additional `ConjugateGradient` minimization (S15) for  $W_{R2}$  as the sum of four monodomain energies, with minimization occurring simultaneously over the 15 parameters of a full second-order twin:

$$W_{R2}(\mathbf{\Lambda}) = \min_{\ell_2, \ell_{11}, \ell_{12} \in \mathcal{D}} f_2 f_{11} W_{NI}(\mathbf{\Lambda}_{11}) + f_2 (1-f_{11}) W_{NI}(\mathbf{\Lambda}_{12}) + (1-f_2) f_{12} W_{NI}(\mathbf{\Lambda}_{21}) + (1-f_2) (1-f_{12}) W_{NI}(\mathbf{\Lambda}_{22}) \tag{S15}$$

This final minimization starts from an initial value of  $(\ell_2, \ell_{11}, \ell_{12}) = (\ell_2(\mathbf{\Lambda}_t), \ell_1(\mathbf{\Lambda}_1), \ell_1(\mathbf{\Lambda}_2))$ , where  $\ell_2$  comes from the grid of micro-structures obtained in the previous  $W_{R2}$  calculation, while  $\ell_1(\mathbf{\Lambda}_1)$  and  $\ell_1(\mathbf{\Lambda}_2)$  are the R1 microstructure interpolation functions evaluated at the deformation gradients in the construction  $\ell_2(\mathbf{\Lambda}_t)$ . In this case, we may indeed

derive the relevant gradients analytically to obtain strong local convergence:

$$\begin{aligned}
\frac{\partial W_{R2}(\mathbf{\Lambda})}{\partial f_2} &= f_{11}W_{NI}(\mathbf{\Lambda}_{11}) + (1 - f_{11})W_{NI}(\mathbf{\Lambda}_{12}) - f_{12}W_{NI}(\mathbf{\Lambda}_{21}) - (1 - f_{12})W_{NI}(\mathbf{\Lambda}_{22}) \\
&\quad - \frac{\mathbf{a}_2 \cdot dW_1 dF_2 \cdot \hat{\mathbf{m}}_2}{1 - f_2} - \frac{\mathbf{a}_2 \cdot dW_2 dF_2 \cdot \hat{\mathbf{m}}_2}{f_2} \\
\frac{\partial W_{R2}(\mathbf{\Lambda})}{\partial n_{\theta 2}} &= \mathbf{a}_2 \cdot (dW_1 dF_2 - dW_2 dF_2) \cdot \frac{\partial \hat{\mathbf{m}}}{\partial \theta} \Big|_{\ell_2} + (dW_1 dF_2 - dW_2 dF_2) \cdot \hat{\mathbf{m}}_2 \cdot \frac{\partial \mathbf{a}}{\partial n_{\theta}} \Big|_{\ell_2} \\
\frac{\partial W_{R2}(\mathbf{\Lambda})}{\partial n_{\phi 2}} &= \mathbf{a}_2 \cdot (dW_1 dF_2 - dW_2 dF_2) \cdot \frac{\partial \hat{\mathbf{m}}}{\partial n_{\phi}} \Big|_{\ell_2} + (dW_1 dF_2 - dW_2 dF_2) \cdot \hat{\mathbf{m}}_2 \cdot \frac{\partial \mathbf{a}}{\partial n_{\phi}} \Big|_{\ell_2} \\
\frac{\partial W_{R2}(\mathbf{\Lambda})}{\partial m_{\phi 2}} &= (dW_1 dF_2 - dW_2 dF_2) \cdot \hat{\mathbf{m}}_2 \cdot \frac{\partial \mathbf{a}}{\partial m_{\phi}} \Big|_{\ell_2} \\
\frac{\partial W_{R2}(\mathbf{\Lambda})}{\partial s_2} &= (dW_1 dF_2 - dW_2 dF_2) \cdot \hat{\mathbf{m}}_2 \cdot \frac{\partial \mathbf{a}}{\partial s} \Big|_{\ell_2}, \\
\frac{\partial W_{R2}(\mathbf{\Lambda})}{\partial f_{11}} &= f_2 W_{NI}(\mathbf{\Lambda}_{11}) - f_2 W_{NI}(\mathbf{\Lambda}_{12}) - \frac{\mathbf{a}_{11} \cdot dW_{11} dF_{11} \cdot \hat{\mathbf{m}}_{11}}{1 - f_{11}} - \frac{\mathbf{a}_{11} \cdot dW_{12} dF_{11} \cdot \hat{\mathbf{m}}_{11}}{f_{11}} \\
\frac{\partial W_{R2}(\mathbf{\Lambda})}{\partial n_{\theta 11}} &= \mathbf{a}_{11} \cdot (dW_{11} dF_{11} - dW_{12} dF_{11}) \cdot \frac{\partial \hat{\mathbf{m}}}{\partial \theta} \Big|_{\ell_{11}} + (dW_{11} dF_{11} - dW_{12} dF_{11}) \cdot \hat{\mathbf{m}}_{11} \cdot \frac{\partial \mathbf{a}}{\partial n_{\theta}} \Big|_{\ell_{11}} \\
\frac{\partial W_{R2}(\mathbf{\Lambda})}{\partial n_{\phi 11}} &= \mathbf{a}_{11} \cdot (dW_{11} dF_{11} - dW_{12} dF_{11}) \cdot \frac{\partial \hat{\mathbf{m}}}{\partial n_{\phi}} \Big|_{\ell_{11}} + (dW_{11} dF_{11} - dW_{12} dF_{11}) \cdot \hat{\mathbf{m}}_{11} \cdot \frac{\partial \mathbf{a}}{\partial n_{\phi}} \Big|_{\ell_{11}} \\
\frac{\partial W_{R2}(\mathbf{\Lambda})}{\partial m_{\phi 11}} &= (dW_{11} dF_{11} - dW_{12} dF_{11}) \cdot \hat{\mathbf{m}}_{11} \cdot \frac{\partial \mathbf{a}}{\partial m_{\phi}} \Big|_{\ell_{11}} \\
\frac{\partial W_{R2}(\mathbf{\Lambda})}{\partial s_{11}} &= (dW_{11} dF_{11} - dW_{12} dF_{11}) \cdot \hat{\mathbf{m}}_{11} \cdot \frac{\partial \mathbf{a}}{\partial s} \Big|_{\ell_{11}}, \\
\frac{\partial W_{R2}(\mathbf{\Lambda})}{\partial f_{12}} &= (1 - f_2)W_{NI}(\mathbf{\Lambda}_{21}) - (1 - f_2)W_{NI}(\mathbf{\Lambda}_{22}) - \frac{\mathbf{a}_{12} \cdot dW_{21} dF_{11} \cdot \hat{\mathbf{m}}_{12}}{1 - f_{12}} - \frac{\mathbf{a}_{12} \cdot dW_{22} dF_{11} \cdot \hat{\mathbf{m}}_{12}}{f_{12}} \\
\frac{\partial W_{R2}(\mathbf{\Lambda})}{\partial n_{\theta 12}} &= \mathbf{a}_{12} \cdot (dW_{21} dF_{11} - dW_{22} dF_{11}) \cdot \frac{\partial \hat{\mathbf{m}}}{\partial \theta} \Big|_{\ell_{12}} + (dW_{21} dF_{11} - dW_{22} dF_{11}) \cdot \hat{\mathbf{m}}_{12} \cdot \frac{\partial \mathbf{a}}{\partial n_{\theta}} \Big|_{\ell_{12}} \\
\frac{\partial W_{R2}(\mathbf{\Lambda})}{\partial n_{\phi 12}} &= \mathbf{a}_{12} \cdot (dW_{21} dF_{11} - dW_{22} dF_{11}) \cdot \frac{\partial \hat{\mathbf{m}}}{\partial n_{\phi}} \Big|_{\ell_{12}} + (dW_{21} dF_{11} - dW_{22} dF_{11}) \cdot \hat{\mathbf{m}}_{12} \cdot \frac{\partial \mathbf{a}}{\partial n_{\phi}} \Big|_{\ell_{12}} \\
\frac{\partial W_{R2}(\mathbf{\Lambda})}{\partial m_{\phi 12}} &= (dW_{21} dF_{11} - dW_{22} dF_{11}) \cdot \hat{\mathbf{m}}_{12} \cdot \frac{\partial \mathbf{a}}{\partial m_{\phi}} \Big|_{\ell_{12}} \\
\frac{\partial W_{R2}(\mathbf{\Lambda})}{\partial s_{12}} &= (dW_{21} dF_{11} - dW_{22} dF_{11}) \cdot \hat{\mathbf{m}}_{12} \cdot \frac{\partial \mathbf{a}}{\partial s} \Big|_{\ell_{12}} \tag{S16}
\end{aligned}$$

where the intermediate derivatives are

$$\begin{aligned}
dW_1 dF_2 &= f_2(1 - f_2) (f_{11} \mathbf{S}(\hat{\mathbf{m}}, (1 - f)\mathbf{a})|_{\ell_{11}} \cdot \mathbf{P}_{NI}(\mathbf{\Lambda}_{11}) \cdot \mathbf{\Lambda}^T + (1 - f_{11}) \mathbf{S}(\hat{\mathbf{m}}, -f\mathbf{a})|_{\ell_{11}} \cdot \mathbf{P}_{NI}(\mathbf{\Lambda}_{12}) \cdot \mathbf{\Lambda}^T) \\
dW_2 dF_2 &= f_2(1 - f_2) (f_{12} \mathbf{S}(\hat{\mathbf{m}}, (1 - f)\mathbf{a})|_{\ell_{12}} \cdot \mathbf{P}_{NI}(\mathbf{\Lambda}_{21}) \cdot \mathbf{\Lambda}^T + (1 - f_{12}) \mathbf{S}(\hat{\mathbf{m}}, -f\mathbf{a})|_{\ell_{12}} \cdot \mathbf{P}_{NI}(\mathbf{\Lambda}_{22}) \cdot \mathbf{\Lambda}^T) \\
dW_{11} dF_{11} &= f_2 f_{11} (1 - f_{11}) (\mathbf{P}_{NI}(\mathbf{\Lambda}_{11}) \mathbf{\Lambda}_1^T) \\
dW_{12} dF_{11} &= f_2 f_{11} (1 - f_{11}) (\mathbf{P}_{NI}(\mathbf{\Lambda}_{12}) \mathbf{\Lambda}_1^T) \\
dW_{21} dF_{11} &= (1 - f_2) f_{12} (1 - f_{12}) (\mathbf{P}_{NI}(\mathbf{\Lambda}_{21}) \mathbf{\Lambda}_2^T) \\
dW_{22} dF_{11} &= (1 - f_2) f_{12} (1 - f_{12}) (\mathbf{P}_{NI}(\mathbf{\Lambda}_{21}) \mathbf{\Lambda}_2^T) \tag{S17}
\end{aligned}$$

and the deformation gradients are

$$\begin{aligned}
\mathbf{\Lambda}_1 &= \mathbf{S}((1 - f)\mathbf{a}, \hat{\mathbf{m}})|_{\ell_2} \mathbf{\Lambda}, \quad \mathbf{\Lambda}_2 = \mathbf{S}(-f\mathbf{a}, \hat{\mathbf{m}})|_{\ell_2} \mathbf{\Lambda}, \\
\mathbf{\Lambda}_{11} &= \mathbf{S}((1 - f)\mathbf{a}, \hat{\mathbf{m}})|_{\ell_{11}} \mathbf{S}((1 - f)\mathbf{a}, \hat{\mathbf{m}})|_{\ell_2} \mathbf{\Lambda}, \quad \mathbf{\Lambda}_{12} = \mathbf{S}(-f\mathbf{a}, \hat{\mathbf{m}})|_{\ell_{12}} \mathbf{S}((1 - f)\mathbf{a}, \hat{\mathbf{m}})|_{\ell_2} \mathbf{\Lambda}, \\
\mathbf{\Lambda}_{21} &= \mathbf{S}((1 - f)\mathbf{a}, \hat{\mathbf{m}})|_{\ell_{21}} \mathbf{S}(-f\mathbf{a}, \hat{\mathbf{m}})|_{\ell_2} \mathbf{\Lambda}, \quad \mathbf{\Lambda}_{22} = \mathbf{S}(-f\mathbf{a}, \hat{\mathbf{m}})|_{\ell_{21}} \mathbf{S}(-f\mathbf{a}, \hat{\mathbf{m}})|_{\ell_2} \mathbf{\Lambda}. \tag{S18}
\end{aligned}$$

Finally, we again interpolate the resulting grid of energies and microstructures in mathematica at cubic order, to give the interpolated functions  $W_{R2}(\mathbf{\Lambda})$  and  $(\ell_2(\mathbf{\Lambda}), \ell_{11}(\mathbf{\Lambda}), \ell_{12}(\mathbf{\Lambda}))$ .

In addition to the two numerical experiments in the main text, we provide a further test of our results, in the well studied “stripe-domain” geometry: an initially relaxed thin sheet with in-plane director, that is stretched perpendicular to  $\mathbf{n}_0$ . More precisely, we consider a planar LCE in the  $x - y$  plane, with  $\mathbf{n}_0 = \hat{\mathbf{y}}$ , so that the minimizing spontaneous distortion is  $\Lambda_s(\hat{\mathbf{y}})$ . We then consider imposing a further perpendicular stretch by  $\lambda$  in the  $\hat{\mathbf{x}}$  direction. Since the sample is thin, it will relax in the thickness direction by an unknown amount  $\lambda_{zz}$ , giving the (incompressible) deformation  $\mathbf{F} = \text{diag}(\lambda, 1/(\lambda_{zz}\lambda), \lambda_{zz})$ . Minimizing over relaxations then gives the relevant energy as

$$W(\lambda) = \min_{\lambda_{zz}} W_{R2}(\text{diag}(\lambda, 1/(\lambda_{zz}\lambda), \lambda_{zz}) \cdot \Lambda_s(\hat{\mathbf{y}})). \quad (\text{S19})$$

This additional relaxation is characteristic of thin sheets and allows a complete analytic solution [S3]. However, here we conduct it as a final minimization step in Mathematica, using our previously computed numerical  $W_{R2}$ . As seen in Fig. S9, this procedure gives energy stress in excellent agreement with the well-established analytic answer [S2]: a stringent test of our numerical relaxation.

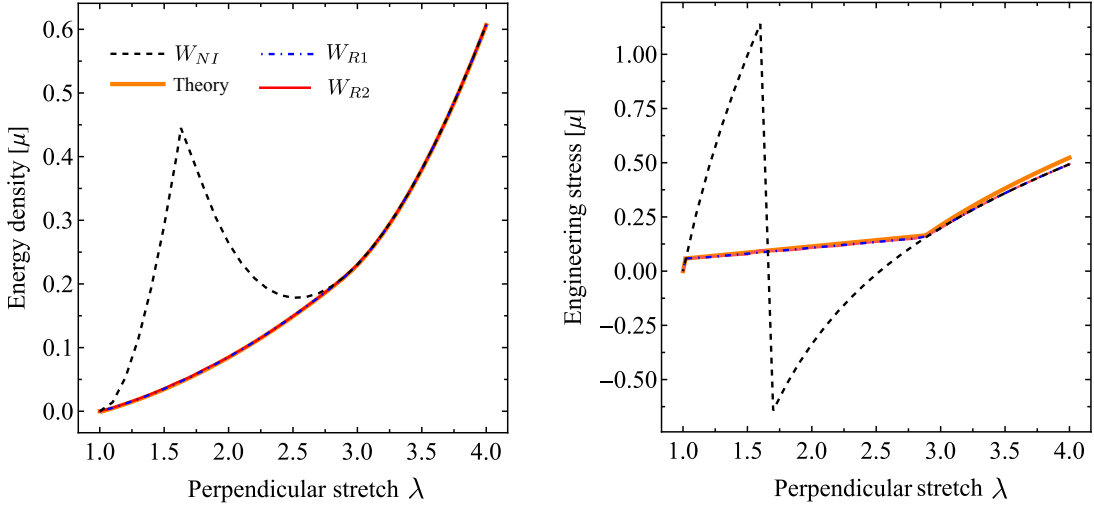


FIG. S9. A benchmark test: stretching perpendicular to  $\mathbf{n}_0$  for  $(\lambda_s, \alpha) = (2, 0.05)$ .

## VI. COMPUTATION OF THE STRESS

To perform finite element simulations, it is necessary to have a constitutive law that describes the relationship between stress and strain for the relaxed energy  $W_{R2}$ . However, obtaining the stress through direct numerical differentiation of  $W_{R2}$  can be challenging due to its numerical nature. Instead, we use an alternative method to calculate the PK1 stress of  $W_{R2}(\mathbf{\Lambda})$  based on the four monodomain variants that make up the second-order twin. The PK1 stress of each of the four variants can be obtained analytically using the equation  $\mathbf{P}_{NI}$  as shown in (S5). The PK1 stress of  $W_{R2}$  is then obtained by taking the volume average of the PK1 stresses of the four variants. This approach enables us to obtain the stress-strain relationship for use in finite element simulations.

We first prove that the PK1 stress of  $W_{R1}$  is the volume average of the PK1 stresses of its variants.

**Theorem 1.** *Suppose*

$$W_{R1}(\mathbf{\Lambda}) = \min_{f \in [0,1], \hat{\mathbf{m}}, \mathbf{a}, \hat{\mathbf{m}}=0} \left( f W_{NI}(\mathbf{\Lambda} + (1-f)\mathbf{a} \otimes \hat{\mathbf{b}}) + (1-f) W_{NI}(\mathbf{\Lambda} - f\mathbf{a} \otimes \hat{\mathbf{b}}) \right) \quad (\text{S20})$$

*is the relaxed energy of the first-order twin. Then the PK1 stresses, computed by taking derivatives of the energy with respect to deformation gradients, satisfy  $\mathbf{P}_{R1}(\mathbf{\Lambda}) = f\mathbf{P}_{NI}(\mathbf{\Lambda}_1) + (1-f)\mathbf{P}_{NI}(\mathbf{\Lambda}_2)$ , equivalently,*

$$\frac{dW_{R1}(\mathbf{\Lambda})}{d\mathbf{\Lambda}} = f \left. \frac{\partial W_{NI}(\mathbf{\Lambda})}{\partial \mathbf{\Lambda}} \right|_{\mathbf{\Lambda}=\mathbf{\Lambda}_1} + (1-f) \left. \frac{\partial W_{NI}(\mathbf{\Lambda})}{\partial \mathbf{\Lambda}} \right|_{\mathbf{\Lambda}=\mathbf{\Lambda}_2} \quad (\text{S21})$$

*where  $\mathbf{\Lambda}_1 = \mathbf{\Lambda} + (1-f)\mathbf{a} \otimes \hat{\mathbf{b}}$  and  $\mathbf{\Lambda}_2 = \mathbf{\Lambda} - f\mathbf{a} \otimes \hat{\mathbf{b}}$  are shears.*

*Proof.* Notice that for a given  $\mathbf{\Lambda}$ , the minimization in (S20) will provide the optimal parameters  $(f, \mathbf{a}, \hat{\mathbf{b}})$  as functions of  $\mathbf{\Lambda}$ . Also, we use the normal  $\hat{\mathbf{b}}$  to the reference twinning plane for simplicity. To simplify the notation, let us define  $W_{R1}(\mathbf{\Lambda})$  as  $g(f(\mathbf{\Lambda}), \mathbf{a}(\mathbf{\Lambda}), \hat{\mathbf{b}}(\mathbf{\Lambda}), \mathbf{\Lambda})$ , where  $g$  represents the right-hand side of (S20) after minimization. Taking the derivative of  $W_{R1}(\mathbf{\Lambda})$  with respect to  $\mathbf{\Lambda}$  yields

$$\frac{dW_{R1}(\mathbf{\Lambda})}{d\mathbf{\Lambda}} = \frac{\partial g}{\partial f} \frac{\partial f}{\partial \mathbf{\Lambda}} + \frac{\partial g}{\partial \mathbf{a}} \cdot \frac{\partial \mathbf{a}}{\partial \mathbf{\Lambda}} + \frac{\partial g}{\partial \hat{\mathbf{b}}} \cdot \frac{\partial \hat{\mathbf{b}}}{\partial \mathbf{\Lambda}} + \frac{\partial g}{\partial \mathbf{\Lambda}}. \quad (\text{S22})$$

Since  $f$ ,  $\mathbf{a}$ , and  $\hat{\mathbf{b}}$  are the minimizers of  $g$ , we have:

$$\frac{\partial g}{\partial f} = 0 \Leftrightarrow W_{NI}(\mathbf{\Lambda}_1) - W_{NI}(\mathbf{\Lambda}_2) + \left( f \frac{\partial W_{NI}}{\partial \mathbf{\Lambda}_1} + (1-f) \frac{\partial W_{NI}}{\partial \mathbf{\Lambda}_2} \right) : (-\mathbf{a} \otimes \hat{\mathbf{b}}) = 0 \quad (\text{S23})$$

$$\frac{\partial g}{\partial \mathbf{a}} = 0 \Leftrightarrow f(1-f) \left( \frac{\partial W_{NI}}{\partial \mathbf{\Lambda}_1} - \frac{\partial W_{NI}}{\partial \mathbf{\Lambda}_2} \right) \hat{\mathbf{b}} = 0 \quad (\text{S24})$$

$$\frac{\partial g}{\partial \hat{\mathbf{m}}} = 0 \Leftrightarrow f(1-f) \mathbf{a} \left( \frac{\partial W_{NI}}{\partial \mathbf{\Lambda}_1} - \frac{\partial W_{NI}}{\partial \mathbf{\Lambda}_2} \right) = 0 \quad (\text{S25})$$

where  $\frac{\partial W_{NI}}{\partial \mathbf{\Lambda}_1} = \frac{\partial W_{NI}(\mathbf{\Lambda})}{\partial \mathbf{\Lambda}} \Big|_{\mathbf{\Lambda}=\mathbf{\Lambda}_1}$  and  $\frac{\partial W_{NI}}{\partial \mathbf{\Lambda}_2} = \frac{\partial W_{NI}(\mathbf{\Lambda})}{\partial \mathbf{\Lambda}} \Big|_{\mathbf{\Lambda}=\mathbf{\Lambda}_2}$ . Physically, Eqs. (S24) and (S25) denote the continuity of force across the twinning plane. Substituting the zero derivatives into (S22), the PK1 stress of  $W_{R1}(\mathbf{\Lambda})$  may be computed by

$$\frac{dW_1(\mathbf{\Lambda})}{d\mathbf{\Lambda}} = \frac{\partial g}{\partial \mathbf{\Lambda}} = f \frac{\partial W_{NI}}{\partial \mathbf{\Lambda}_1} + (1-f) \frac{\partial W_{NI}}{\partial \mathbf{\Lambda}_2}. \quad (\text{S26})$$

This completes the proof.  $\square$

An immediate generalization of Eq. S21 implies that the PK1 stress for  $W_{R2}(\mathbf{\Lambda})$  may be obtained by averaging the PK1 stresses of the four variants:

$$\mathbf{P}_{R2}(\mathbf{\Lambda}) = f_2 f_{11} \mathbf{P}_{NI}(\mathbf{\Lambda}_{11}) + f_2 (1-f_{11}) \mathbf{P}_{NI}(\mathbf{\Lambda}_{12}) + (1-f_2) f_{12} \mathbf{P}_{NI}(\mathbf{\Lambda}_{21}) + (1-f_2)(1-f_{12}) \mathbf{P}_{NI}(\mathbf{\Lambda}_{22}), \quad (\text{S27})$$

where the four deformations  $\mathbf{\Lambda}_{11}$ ,  $\mathbf{\Lambda}_{12}$ ,  $\mathbf{\Lambda}_{21}$  and  $\mathbf{\Lambda}_{22}$  are obtained from  $W_{R2}(\mathbf{\Lambda})$ . In the numerical relaxation, we calculate the PK1 stress solely for the test deformation gradient  $\mathbf{\Lambda}_t$ . Subsequently, we use interpolation to generate a PK1 stress function  $\mathbf{P}_{PK1}(\Lambda_1, \Lambda_3, \theta, \phi)$  that corresponds to the test deformation gradient. To obtain the PK1 stress for an arbitrary  $\mathbf{\Lambda}$  that matches the parameters of  $\mathbf{\Lambda}_t$ , we identify two orthogonal transformations  $\mathbf{R}_1$  and  $\mathbf{R}_2$  that satisfy  $\mathbf{\Lambda} = \mathbf{R}_1 \mathbf{\Lambda}_t \mathbf{R}_2$ . Then, we calculate the PK1 stress for  $\mathbf{\Lambda}$  as  $\mathbf{P}_{R2}(\mathbf{\Lambda}) = \mathbf{R}_1 \mathbf{P}_{PK1}(\Lambda_1, \Lambda_3, \theta, \phi) \mathbf{R}_2$ . Accordingly, the Cauchy stress is given by  $\boldsymbol{\sigma}_{R2} = \mathbf{P}_{R2}(\mathbf{\Lambda}) \mathbf{\Lambda}^T$  in the incompressible regime.

## VII. FINITE ELEMENT METHOD

We use the damped Newton dynamics and finite element method from [S5] in our simulation. In order to provide a self-contained description of our numerical simulation of instability, we briefly outline it in this paper.

The LCE slab is modeled as a compressible elastomer with a bulk modulus of  $B = 100\mu$ , allowing for slight compressibility. Our total elastic energy  $E$  comprises three components: the  $W_{R2}$  energy of LCE, the neo-Hookean energy, and the bulk energy. In particular, allowing the compressibility, we obtain:

$$E = f W_{R2}(\mathbf{\Lambda} J^{-1/3}) + (1-f) \frac{\mu}{2} \left[ \text{Tr}(\mathbf{\Lambda} \mathbf{\Lambda}^T J^{-2/3}) - 3 \right] + B(J-1)^2. \quad (\text{S28})$$

Here,  $f \in [0, 1]$  represents the fraction of LCE energy, and  $J = \text{Det} \mathbf{\Lambda}$ . The corresponding Cauchy stress  $\boldsymbol{\sigma}_{el}$  is composed of three components: the LCE stress  $\boldsymbol{\sigma}_L$ , the neo-Hookean stress  $\boldsymbol{\sigma}_N$ , and the bulk pressure  $\boldsymbol{\sigma}_B$ . In the compressible regime, the three stresses are given by:

$$\boldsymbol{\sigma}_L = \left[ \tilde{\mathbf{P}}_2 \mathbf{\Lambda}^T - \frac{1}{3} \text{Tr}(\tilde{\mathbf{P}}_2 \mathbf{\Lambda}^T) \mathbf{I} \right] J^{-4/3} \quad (\text{S29})$$

$$\boldsymbol{\sigma}_N = \mu \left[ \mathbf{\Lambda} \mathbf{\Lambda}^T - \frac{1}{3} \text{Tr}(\mathbf{\Lambda} \mathbf{\Lambda}^T) \mathbf{I} \right] J^{-5/3} \quad (\text{S30})$$

$$\boldsymbol{\sigma}_B = B(J-1) \mathbf{I} \quad (\text{S31})$$

respectively, where  $\tilde{\mathbf{P}}_2 = \mathbf{P}_{R2}(\mathbf{\Lambda}J^{-1/3})$  is the PK1 stress for  $W_{R2}$  evaluated at the revised deformation gradient  $\mathbf{\Lambda}J^{-1/3}$  with unity determinant. Then the total Cauchy stress is the sum of the three terms:

$$\boldsymbol{\sigma}_{el} = f\boldsymbol{\sigma}_L + (1-f)\boldsymbol{\sigma}_N + \boldsymbol{\sigma}_B. \quad (\text{S32})$$

To compute the equilibrium configuration, we also assume that each element has internal viscous stress  $\boldsymbol{\sigma}_\eta$ . Finally, the total stress  $\boldsymbol{\sigma}$  for each element may be given by

$$\boldsymbol{\sigma} = \boldsymbol{\sigma}_{el} + \boldsymbol{\sigma}_\eta. \quad (\text{S33})$$

As shown in Fig. S10, each cubic element consists of three tetrahedrons. The deformation gradient is given by  $\mathbf{\Lambda} = (\mathbf{y}_1 - \mathbf{y}_0, \mathbf{y}_2 - \mathbf{y}_0, \mathbf{y}_3 - \mathbf{y}_0)(\mathbf{x}_1 - \mathbf{x}_0, \mathbf{x}_2 - \mathbf{x}_0, \mathbf{x}_3 - \mathbf{x}_0)^{-1}$  and the viscous stress by  $\boldsymbol{\sigma}_\eta = \eta(\mathbf{\Lambda} + \dot{\mathbf{\Lambda}}^T)/2$

The surface traction at each face of the tetrahedron is determined by  $-\boldsymbol{\sigma}\mathbf{n}_i$ , and the nodal forces  $\mathbf{f}$  are obtained by distributing the surface traction equally among the three corresponding nodes. Specifically, the total force  $\mathbf{f}$  applied to a node is the sum of the elastic nodal force  $\mathbf{f}_n$  and the damping force  $\mathbf{f}_d$  given by:

$$\mathbf{f} = \mathbf{f}_n + \mathbf{f}_d, \quad (\text{S34})$$

where  $\mathbf{f}_d = -\gamma\mathbf{v}$ ,  $\gamma$  is the damping coefficient, and  $\mathbf{v}$  is the velocity of the node. In the FE simulation, at time  $t$ , each node's position  $\mathbf{x}(t)$  and velocity  $\mathbf{v}(t)$  are updated using the damped Newton dynamics:

$$\begin{aligned} \mathbf{v}(t + \Delta t) &= \mathbf{v}(t) + \frac{\mathbf{f}_n(t) - \gamma\mathbf{v}(t)}{m}, \\ \mathbf{x}(t + \Delta t) &= \mathbf{x}(t) + \mathbf{v}(t + \Delta t). \end{aligned} \quad (\text{S35})$$

Here  $\Delta t = 0.2a\sqrt{\rho/B}$  is the time step,  $m = \rho a^3$  is the nodal mass, and  $\rho = 1$  is the density. For more details about the FE method, we refer the reader to the supplement of [S5].

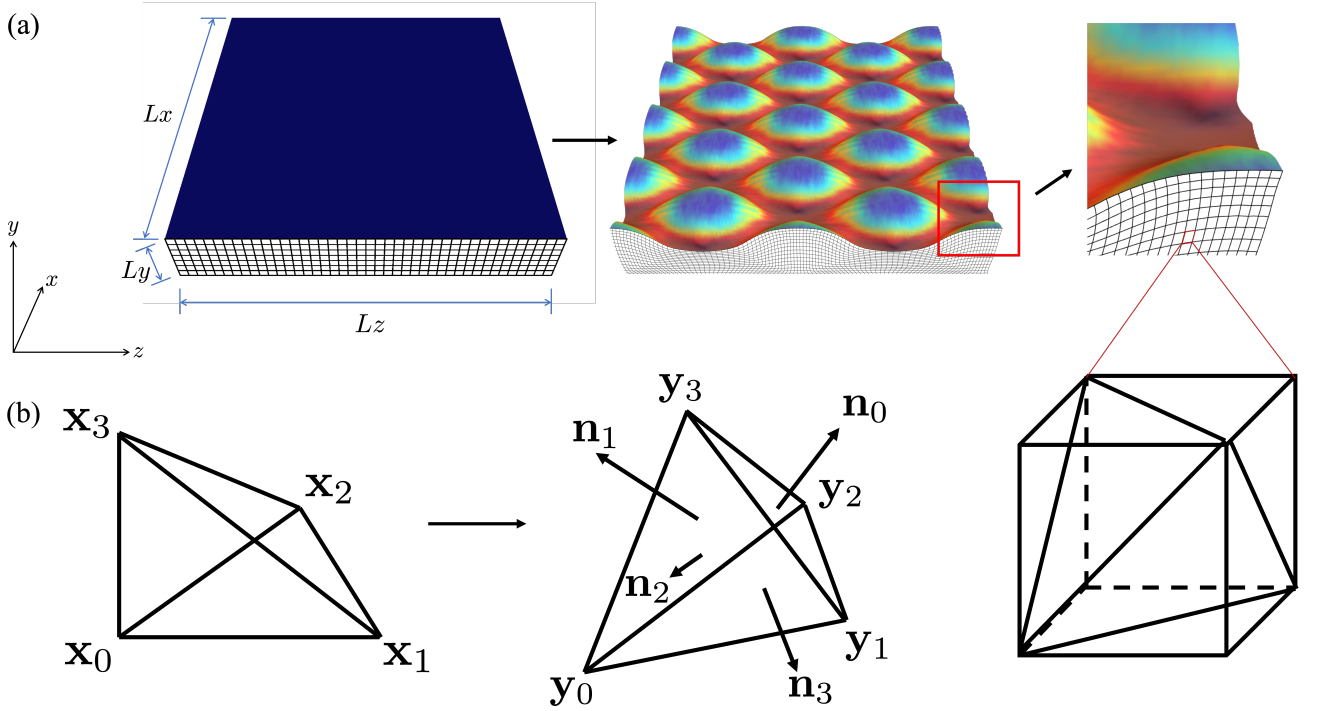


FIG. S10. (a) The simulation is initialized for an LCE slab at the isotropic state. As cooling to the nematic state, the surface instability is triggered and simulated by FEM. Each cuboid element has nine tetrahedrons. (b) The reference and deformed tetrahedrons and the surface normals.

## VIII. NUMERICAL SIMULATION RESULTS

We simulate a cuboid-shaped domain with dimensions  $L_x \times L_y \times L_z$  as depicted in Fig. S10(a). The thickness direction is represented by  $y$ , and the number of nodes in each dimension is  $n_x$ ,  $n_y$ , and  $n_z$ , respectively. We employ

periodic boundary condition along  $x$  and  $z$ , free boundary at the top, and clamped boundary at the bottom. The preferred director  $\mathbf{n}_0$  is aligned along  $x$ . The simulation of the LCE slab starts from the isotropic state and is then cooled to the nematic state driven by the  $W_{R2}$  energy.

Before conducting the simulation, we validated the mesh size dependence and found that convergence could only be achieved when the number of nodes in  $L_y$  exceeded 30 (Fig. S11(a)). The  $W_{R2}$  energy is transversely isotropic, resulting in a 2D periodic pattern in the equilibrium state. However, unlike neo-Hookean material, the periodicities along  $y$  and  $z$  in the equilibrium configuration of LCEs are different, making it challenging to determine the wavelength for the energy-minimizing state. To address this issue, we first simulated a large domain with dimensions  $10h \times h \times 10h$  to roughly estimate the wavelengths  $\tilde{a}_1$  and  $\tilde{a}_3$  along  $x$  and  $z$ . Next, we conducted nine calibrated simulations with a finer mesh. We set the simulated domains  $b_1 \times h \times b_3$  to be adjacent to  $\tilde{a}_1 \times h \times \tilde{a}_3$ , specifically  $b_1 \times h \times b_3 = (\tilde{a}_1 - 0.1h, \tilde{a}_1, \tilde{a}_1 + 0.1h) \times h \times (\tilde{a}_3 - 0.1h, \tilde{a}_3, \tilde{a}_3 + 0.1h)$ . We plotted the simulated energy densities (energy per unit reference volume) against  $(b_1, b_3)$  in Fig.S11(b), which formed a convex envelope including an energy minimum. If the energy minimum point was not included, we adjusted  $(\tilde{a}_1, \tilde{a}_3)$  and repeated the process. We then interpolated the energy density to determine the optimal wavelengths  $(a_1, a_3)$  along  $x$  and  $z$  corresponding to the energy minimum. Finally, we simulated the equilibrium state of the domain size  $(a_1, h, a_3)$  with a finer mesh and then periodically translated it to obtain a larger domain for illustration.

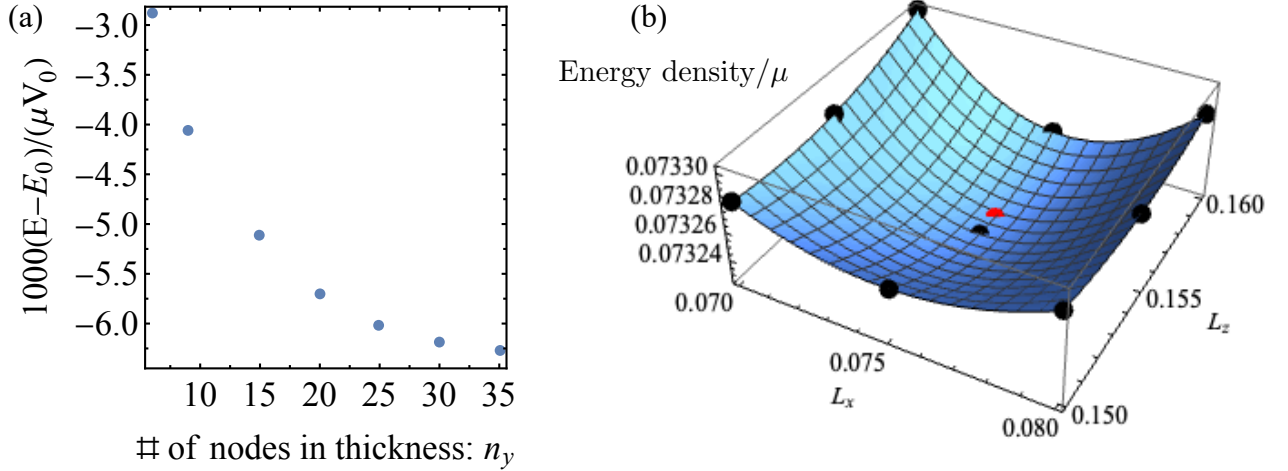


FIG. S11. Mesh validation and energy interpolation.

We provide the simulation details for Fig. 4 in Table S1 and more views in Fig. S12. Simulations #1, #2, #3, and #4 were conducted to explore the impact of  $\alpha$ , while simulations #4, #5, and #6 were conducted to examine the effect of  $\lambda_s$ . Simulation #0 was performed with a coarse mesh and large domain to investigate the dynamics and coarsening of the instability shown in Fig. 4(a).

#	$\lambda_s$	$\alpha$	$L_x$	$L_y$	$L_z$	$n_x$	$n_y$	$n_z$
0	2	0.05	0.3	0.05	0.312	91	15	93
1	1.44	0.05	0.073	0.05	0.157	43	31	91
2	1.71	0.05	0.075	0.05	0.155	45	31	93
3	2	0.05	0.075	0.05	0.156	51	35	107
4	2.15	0.05	0.07	0.05	0.15	41	31	87
5	2.15	0.15	0.066	0.05	0.172	41	31	101
6	2.15	0.3	0.055	0.05	0.162	34	31	98

TABLE S1. Simulation details for Fig. (4) in the main text.

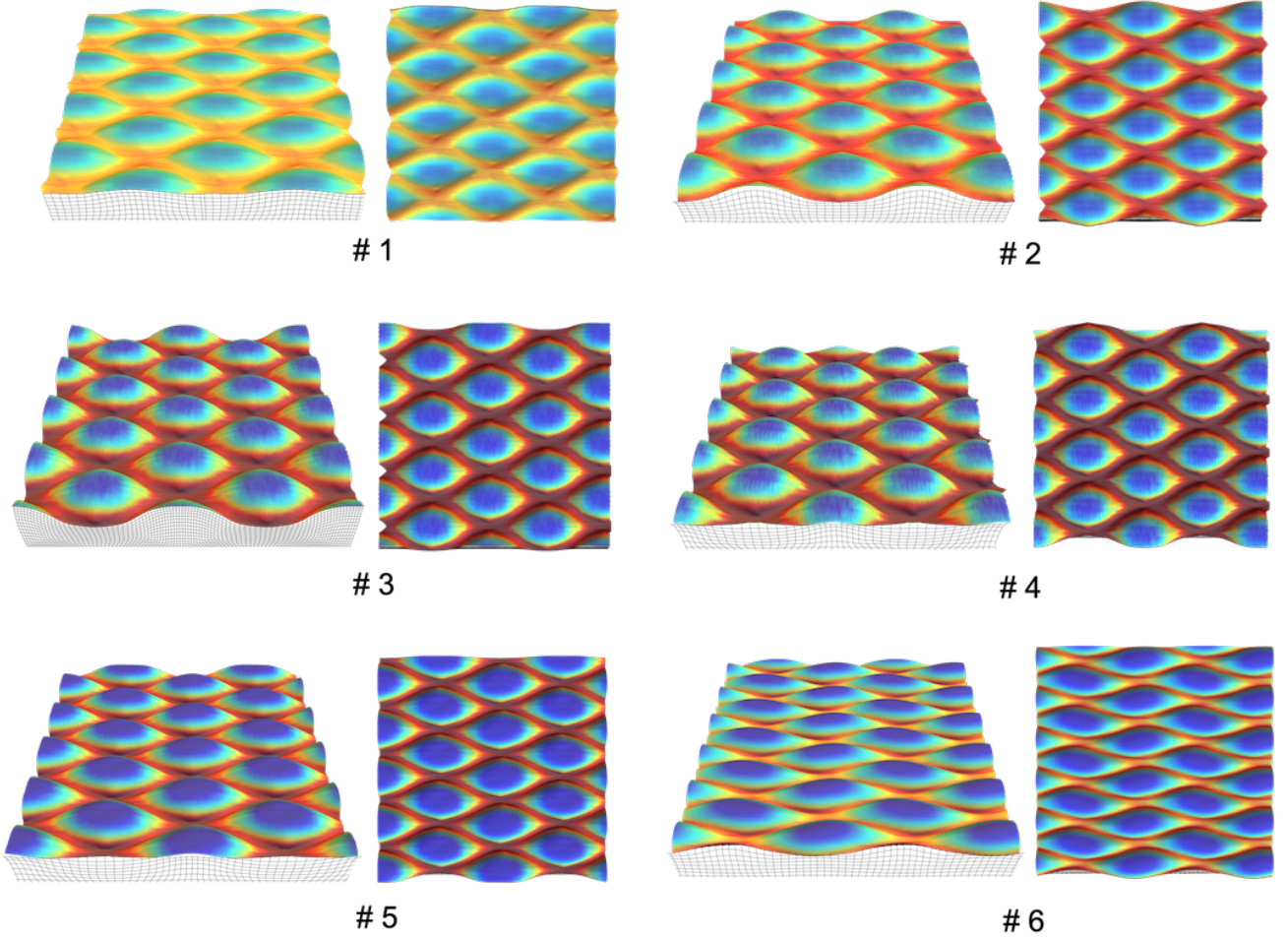


FIG. S12. Side view and top view of simulations in Table. S1.

### IX. LINEAR STABILITY ANALYSIS

Many biological tissues and fiber-reinforced composites are examples of transversely isotropic materials. Unlike isotropic materials, the mechanical response of transversely isotropic materials remains the same under rotations about a preferred axis. Therefore, a general strain-energy function with four invariants is required to model the mechanical response of such materials if they are incompressible [S6]. The use of a strain-energy function with four invariants also makes the linear stability analysis more challenging due to the reduction of symmetry. Non-ideal LCE is an example of a transversely isotropic material, with  $\mathbf{n}_0$  as the preferred axis. In this section, we present some general results of linear stability analysis for transversely isotropic materials and a semi-theoretical linear stability analysis for our LCE instability problem using the numerical relaxed LCE energy  $W_{R2}$ .

Let the elastic energy for a transversely isotropic material be  $W_N(\mathbf{\Lambda})$ . Following the free top surface condition, we vary the deformation gradient to its first order  $\mathbf{\Lambda} = \mathbf{\Lambda}^0 + \epsilon \mathbf{\Lambda}^1$ , where  $\mathbf{\Lambda}^0 = \mathbf{I} + \gamma \hat{\mathbf{z}} \otimes \hat{\mathbf{z}}$  is the base state. Then we perturb the energy at its base state and get

$$W_N(\mathbf{\Lambda}) = W_N(\mathbf{\Lambda}_0) + \left. \frac{\partial^2 W_N}{\partial \Lambda_{ij} \partial \Lambda_{kl}} \right|_{\mathbf{\Lambda}_0} \Lambda_{ij}^1 \Lambda_{kl}^1. \quad (\text{S36})$$

Taking the variation of (S36) yields the balance of force equation  $\partial_i P_{ij} = 0$ , where

$$P_{ij} = \left. \frac{\partial^2 W_N}{\partial \Lambda_{ij} \partial \Lambda_{kl}} \right|_{\mathbf{\Lambda}_0} \Lambda_{kl}^1. \quad (\text{S37})$$

Owing to the uniaxial symmetry of  $W_N(\mathbf{\Lambda})$ , many of the second-order derivatives are zero. To compute this, we may write a general energy form  $W_N(\mathbf{\Lambda})$  for a transversely isotropic material as [S6]

$$W_N(\mathbf{\Lambda}) = g \left( \text{Tr}(\mathbf{\Lambda}\mathbf{\Lambda}^T), \text{Tr}[(\mathbf{\Lambda}\mathbf{\Lambda}^T)^{-1}], \mathbf{\Lambda}\mathbf{n}_0 \cdot \mathbf{\Lambda}\mathbf{n}_0, \mathbf{\Lambda}^T \mathbf{\Lambda}\mathbf{n}_0 \cdot \mathbf{\Lambda}^T \mathbf{\Lambda}\mathbf{n}_0, \text{Det}\mathbf{\Lambda} \right), \quad (\text{S38})$$

where  $\mathbf{n}_0 = \mathbf{e}_1$  is the preferred direction. Here we define  $\mathbf{e}_1 = \hat{\mathbf{x}}$ ,  $\mathbf{e}_2 = \hat{\mathbf{y}}$ ,  $\mathbf{e}_3 = \hat{\mathbf{z}}$ . Let  $W_N^{\mathbf{e}_i \otimes \mathbf{e}_j + \mathbf{e}_k \otimes \mathbf{e}_l}$  denote the second-order derivative  $\frac{\partial^2 W_N}{\partial \Lambda_{ij} \partial \Lambda_{kl}}$ . For example,  $W_N^{((1,1,0),(0,0,0),(0,0,0))}$  denotes the second-order derivative  $\frac{\partial^2 W_N}{\partial \Lambda_{11} \partial \Lambda_{12}}$ . Taking the second-order derivative directly yields 15 non-zero second-order derivatives corresponding to

$$\begin{aligned} & \mathbf{e}_i \otimes \mathbf{e}_j + \mathbf{e}_k \otimes \mathbf{e}_l = \\ & \left\{ \begin{array}{lll} ((2, 0, 0), (0, 0, 0), (0, 0, 0)), & ((1, 0, 0), (0, 1, 0), (0, 0, 0)), & ((1, 0, 0), (0, 0, 0), (0, 0, 1)), \\ ((0, 2, 0), (0, 0, 0), (0, 0, 0)), & ((0, 1, 0), (1, 0, 0), (0, 0, 0)), & ((0, 0, 2), (0, 0, 0), (0, 0, 0)), \\ ((0, 0, 1), (0, 0, 0), (1, 0, 0)), & ((0, 0, 0), (2, 0, 0), (0, 0, 0)), & ((0, 0, 0), (0, 2, 0), (0, 0, 0)), \\ ((0, 0, 0), (0, 1, 0), (0, 0, 1)), & ((0, 0, 0), (0, 0, 2), (0, 0, 0)), & ((0, 0, 0), (0, 0, 1), (0, 1, 0)), \\ ((0, 0, 0), (0, 0, 0), (2, 0, 0)), & ((0, 0, 0), (0, 0, 0), (0, 2, 0)), & ((0, 0, 0), (0, 0, 0), (0, 0, 2)). \end{array} \right. \quad (\text{S39}) \end{aligned}$$

To solve the variational equation  $\partial_i P_{ij} = 0$ , we substitute a test perturbed field that exponentially decays in  $z$  as  $\mathbf{\Lambda}^1 = \mathbf{v}(x, y) \exp(k\lambda z)$ . The  $xy$  field  $\mathbf{v}(x, y)$  has a wave vector  $\mathbf{k}$  along  $\hat{\mathbf{x}}'$  that makes an oblique angle  $\theta$  to  $\hat{\mathbf{x}}$ , resulting in

$$\mathbf{v}(x, y) = c_h \cos(kx') \hat{\mathbf{x}}' + c_g \cos(kx') \hat{\mathbf{y}}' + \sin(kx') \hat{\mathbf{z}}. \quad (\text{S40})$$

Substituting  $\mathbf{\Lambda}^1$  into the variational equation yields three equations linear in  $c_h$  and  $c_g$  but quadratic in  $\lambda$ , which are Equation EL(1):

$$\begin{aligned} & \lambda^2 \left( \sin \theta (c_g \cos \theta + c_h \sin \theta) W_N^{((0,0,0),(0,0,0),(0,2,0))} + \cos \theta (c_h \cos \theta - c_g \sin \theta) W_N^{((0,0,0),(0,0,0),(2,0,0))} \right) \\ & + \lambda \left( \sin^2 \theta (W_N^{((0,0,0),(0,0,1),(0,1,0))} + W_N^{((0,0,0),(0,1,0),(0,0,1))}) + \cos^2 \theta (W_N^{((0,0,1),(0,0,0),(1,0,0))} + W_N^{((1,0,0),(0,0,0),(0,0,1))}) \right) \\ & + (-c_g \sin^3 \theta \cos \theta - c_h \sin^4 \theta) W_N^{((0,0,0),(0,2,0),(0,0,0))} + (c_g \sin^3 \theta \cos \theta - c_h \sin^2 \theta \cos^2 \theta) W_N^{((0,0,0),(2,0,0),(0,0,0))} \\ & + (-c_g \sin \theta \cos^3 \theta + c_g \sin^3 \theta \cos \theta - 2c_h \sin^2 \theta \cos^2 \theta) W_N^{((0,1,0),(1,0,0),(0,0,0))} \\ & + (-c_g \sin \theta \cos^3 \theta - c_h \sin^2 \theta \cos^2 \theta) W_N^{((0,2,0),(0,0,0),(0,0,0))} \\ & + (-c_g \cos \theta^3 \sin \theta - 2c_h \cos \theta^2 \sin \theta^2 + c_g \cos \theta \sin \theta^3) W_N^{((1,0,0),(0,1,0),(0,0,0))} \\ & + \cos \theta^3 (-c_h \cos \theta + c_g \sin \theta) W_N^{((2,0,0),(0,0,0),(0,0,0))} = 0, \quad (\text{S41}) \end{aligned}$$

Equation EL(2):

$$\begin{aligned} & \lambda^2 \left( -\cos \theta (\cos \theta c_g + c_h \sin \theta) W_N^{((0,0,0),(0,0,0),(0,2,0))} + \sin \theta (\cos \theta c_h - c_g \sin \theta) W_N^{((0,0,0),(0,0,0),(2,0,0))} \right) \\ & + \lambda \cos \theta \sin \theta \left( -W_N^{((0,0,0),(0,0,1),(0,1,0))} - W_N^{((0,0,0),(0,1,0),(0,0,1))} + W_N^{((0,0,1),(0,0,0),(1,0,0))} + W_N^{((1,0,0),(0,0,0),(0,0,1))} \right) \\ & + (c_g \cos \theta^2 \sin \theta^2 + c_h \cos \theta \sin \theta^3) W_N^{((0,0,0),(0,2,0),(0,0,0))} + (-c_h \cos \theta \sin \theta^3 + c_g \sin \theta^4) W_N^{((0,0,0),(2,0,0),(0,0,0))} \\ & + (c_h \cos \theta^3 \sin \theta - 2c_g \cos \theta^2 \sin \theta^2 - c_h \cos \theta \sin \theta^3) W_N^{((0,1,0),(1,0,0),(0,0,0))} \\ & + (c_g \cos \theta^4 + c_h \cos \theta^3 \sin \theta) W_N^{((0,2,0),(0,0,0),(0,0,0))} \\ & + (c_h \cos \theta^3 \sin \theta - 2c_g \cos \theta^2 \sin \theta^2 - c_h \cos \theta \sin \theta^3) W_N^{((1,0,0),(0,1,0),(0,0,0))} \\ & + \cos \theta^2 \sin \theta (-c_h \cos \theta + c_g \sin \theta) W_N^{((2,0,0),(0,0,0),(0,0,0))} = 0, \quad (\text{S42}) \end{aligned}$$

Equation EL(3):

$$\begin{aligned} & \lambda^2 W_N^{((0,0,0),(0,0,0),(0,0,2))} \\ & + \lambda \left( -\sin \theta (c_g \cos \theta + c_h \sin \theta) W_N^{((0,0,0),(0,0,1),(0,1,0))} - c_g \cos \theta \sin \theta W_N^{((0,0,0),(0,1,0),(0,0,1))} \right. \\ & - c_h \sin \theta^2 W_N^{((0,0,0),(0,1,0),(0,0,1))} - c_h \cos \theta^2 W_N^{((0,0,1),(0,0,0),(1,0,0))} \\ & \left. + c_g \cos \theta \sin \theta W_N^{((0,0,1),(0,0,0),(1,0,0))} + \cos \theta (-c_h \cos \theta + c_g \sin \theta) W_N^{((1,0,0),(0,0,0),(0,0,1))} \right) \\ & - \sin \theta^2 W_N^{((0,0,0),(0,0,2),(0,0,0))} - \cos \theta^2 W_N^{((0,0,2),(0,0,0),(0,0,0))} = 0. \quad (\text{S43}) \end{aligned}$$

Generically, all 15 second-order derivatives are non-zero. After solving for the coefficients  $c_h$  and  $c_g$ , the equilibrium equation  $\partial_i P_{ij} = 0$  (i.e., equations EL(1), EL(2) and EL(3)) yields a cubic polynomial in  $\lambda^2$ . By selecting the decaying solutions in  $-y$ , we may obtain three positive roots  $\lambda = \lambda_1, \lambda_2, \lambda_3$ , three corresponding pairs of coefficients  $(c_{g1}, c_{h1})$ ,  $(c_{g2}, c_{h2})$ ,  $(c_{g3}, c_{h3})$ , and three perturbed fields,  $\mathbf{\Lambda}_{(1)}^1$ ,  $\mathbf{\Lambda}_{(2)}^1$ , and  $\mathbf{\Lambda}_{(3)}^1$ . The total field can be expressed as the linear combination:

$$\mathbf{\Lambda}^1 = c_1 \mathbf{\Lambda}_{(1)}^1 + c_2 \mathbf{\Lambda}_{(2)}^1 + c_3 \mathbf{\Lambda}_{(3)}^1. \quad (\text{S44})$$

Then we substitute the perturbation mode  $\mathbf{\Lambda}^1$  back into the energy density equation (S36), and integrate over a period  $\hat{x}' \in [0, 2\pi/k]$  to obtain

$$\begin{aligned} & \int_0^{2\pi/k} \frac{\partial^2 W_N}{\partial \Lambda_{ij} \partial \Lambda_{kl}} \Big|_{\mathbf{\Lambda}_0} \Lambda_{ij}^1 \Lambda_{kl}^1 dx' = \\ & \pi f_z'^2 (W_N^{((0,0,0),(0,0,0),(0,0,2))}) / (2k) + \pi (\sin \theta f_x' + \cos \theta f_y')^2 W_N^{((0,0,0),(0,0,0),(0,2,0))} / (2k) \\ & + \pi (\cos \theta f_x' - \sin \theta f_y')^2 W_N^{((0,0,0),(0,0,0),(2,0,0))} / (2k) + \pi f_z \sin \theta (\sin \theta f_x' + \cos \theta f_y') W_N^{((0,0,0),(0,0,1),(0,1,0))} \\ & + 1/2k\pi f_z^2 \sin^2 \theta W_N^{((0,0,0),(0,0,2),(0,0,0))} - \pi \sin \theta (\cos \theta f_y + f_x \sin \theta) f_z' W_N^{((0,0,0),(0,1,0),(0,0,1))} \\ & + 1/2k\pi \sin^2 \theta (\cos \theta f_y + f_x \sin \theta)^2 W_N^{((0,0,0),(0,2,0),(0,0,0))} + 1/2k\pi \sin^2 \theta (\cos \theta f_x - f_y \sin \theta)^2 W_N^{((0,0,0),(2,0,0),(0,0,0))} \\ & + \pi \cos \theta f_z (\cos \theta f_x' - \sin \theta f_y') W_N^{((0,0,1),(0,0,1),(1,0,0))} + 1/2k\pi \cos^2 \theta f_z^2 W_N^{((0,0,2),(0,0,0),(0,0,0))} \\ & + k\pi \cos \theta \sin \theta (\cos \theta f_y + f_x \sin \theta) (\cos \theta f_x - f_y \sin \theta) W_N^{((0,1,0),(1,0,0),(0,0,0))} \\ & + 1/2k\pi \cos^2 \theta (\cos \theta f_y + f_x \sin \theta)^2 W_N^{((0,2,0),(0,0,0),(0,0,0))} \\ & - \pi \cos \theta (\cos \theta f_x - f_y \sin \theta) f_z' W_N^{((1,0,0),(0,0,0),(0,0,1))} \\ & + k\pi \cos \theta \sin \theta (\cos \theta f_y + f_x \sin \theta) (\cos \theta f_x - f_y \sin \theta) W_N^{((1,0,0),(0,1,0),(0,0,0))} \\ & + 1/2k\pi \cos^2 \theta (\cos \theta f_x - f_y \sin \theta)^2 W_N^{((2,0,0),(0,0,0),(0,0,0))} \end{aligned} \quad (\text{S45})$$

where  $f_x(z) = c_1 c_{h1} \exp(k\lambda_1 z) + c_2 c_{h2} \exp(k\lambda_2 z) + c_3 c_{h3} \exp(k\lambda_3 z)$ ,  $f_y(z) = c_1 c_{g1} \exp(k\lambda_1 z) + c_2 c_{g2} \exp(k\lambda_2 z) + c_3 c_{g3} \exp(k\lambda_3 z)$  and  $f_z(z) = c_1 \exp(k\lambda_1 z) + c_2 \exp(k\lambda_2 z) + c_3 \exp(k\lambda_3 z)$ . Then integrating upon the depth  $z \in (-\infty, 0]$  yields a quadratic form of the coefficients  $c_1$ ,  $c_2$ , and  $c_3$ . To determine stability, we calculate the minimum eigenvalue of the resulting Hessian matrix. A negative eigenvalue indicates instability. In the range  $\theta \in [0, \pi/2]$ , the smallest negative eigenvalue corresponds to the fastest decay in energy.

**LCE + neo-Hookean case.** The combination of LCE and neo-Hookean energy has the form

$$W_N(\mathbf{\Lambda}) = f W_{R2}(\mathbf{\Lambda}/\text{Det}\mathbf{\Lambda}) + (1-f) W_{NH}(\mathbf{\Lambda}/\text{Det}\mathbf{\Lambda}) + B(\text{Det}\mathbf{\Lambda} - 1)^2/2. \quad (\text{S46})$$

We consider an example with energy at the critical volume fraction  $f = f_c = 0.963$ . The base state  $\mathbf{\Lambda}_0 = \mathbf{I} + \gamma \hat{\mathbf{z}} \otimes \hat{\mathbf{z}}$  satisfies the top free surface condition, i.e.,  $\frac{\partial W_N}{\partial \mathbf{\Lambda}} \Big|_{\mathbf{\Lambda}=\mathbf{\Lambda}_0} \hat{\mathbf{z}} = 0$ , resulting in  $\gamma = -0.0006544$ . We then evaluate the derivatives at the base state:

$$\begin{cases} W_N^{((2,0,0),(0,0,0),(0,0,0))} = 100.2039, & W_N^{((1,0,0),(0,1,0),(0,0,0))} = 99.7018, & W_N^{((1,0,0),(0,0,0),(0,0,1))} = 99.7671, \\ W_N^{((0,2,0),(0,0,0),(0,0,0))} = 0.2333, & W_N^{((0,1,0),(1,0,0),(0,0,0))} = 0.2332, & W_N^{((0,0,2),(0,0,0),(0,0,0))} = 0.2336, \\ W_N^{((0,0,1),(0,0,0),(1,0,0))} = 0.2334, & W_N^{((0,0,0),(2,0,0),(0,0,0))} = 0.03702, & W_N^{((0,0,0),(0,2,0),(0,0,0))} = 99.8917, \\ W_N^{((0,0,0),(0,1,0),(0,0,1))} = 99.8831, & W_N^{((0,0,0),(0,0,2),(0,0,0))} = 0.03702, & W_N^{((0,0,0),(0,0,1),(0,1,0))} = 0.03699, \\ W_N^{((0,0,0),(0,0,0),(2,0,0))} = 0.03702, & W_N^{((0,0,0),(0,0,0),(0,2,0))} = 0.03702, & W_N^{((0,0,0),(0,0,0),(0,0,2))} = 100.0226. \end{cases} \quad (\text{S47})$$

The perturbed field at  $\theta = 0.327\pi$  is

$$\begin{aligned} \mathbf{\Lambda}_{(1)}^1 &= 1.0429 \exp(1.0430z) \hat{\mathbf{x}}' - 0.1377 \exp(1.0430z) \hat{\mathbf{y}}' + \exp(1.0430z) \hat{\mathbf{z}}, \\ \mathbf{\Lambda}_{(2)}^1 &= 1.4182 \exp(1.4181z) \hat{\mathbf{x}}' - 1.1722 \exp(1.4181z) \hat{\mathbf{y}}' + \exp(1.4181z) \hat{\mathbf{z}}, \\ \mathbf{\Lambda}_{(3)}^1 &= 1.5578 \exp(1.5568z) \hat{\mathbf{x}}' + 0.9471 \exp(1.5568z) \hat{\mathbf{y}}' + \exp(1.5568z) \hat{\mathbf{z}}. \end{aligned} \quad (\text{S48})$$

The energy expression obtained is quadratic and can be written as follows:

$$E = 0.5341c_1^2 + 1.0990c_2^2 + c_1(1.5216c_2 + 0.9636c_3) + 1.2808c_2c_3 + 0.5717c_3^2. \quad (\text{S49})$$

To determine stability, we calculate the minimum eigenvalue of the Hessian matrix, which is found to be  $-0.00009$ . This value is just below zero, indicating a marginally unstable system.

**Pure LCE case.** In the pure LCE case, owing to the evolution of the second-order twin, three additional second-order derivatives,  $W_N^{((0,0,0),(0,0,2),(0,0,0))}$ ,  $W_N^{((0,0,0),(0,0,0),(0,2,0))}$  and  $W_N^{((0,0,0),(0,0,1),(0,1,0))}$  are zero. The underlying mechanism is that by forming the second-order twin, the shear  $(\mathbf{I} + s(\mathbf{n}_0 \times \mathbf{n}_0^\perp) \otimes \mathbf{n}_0^\perp)$  will induce changes of volume fractions but preserve the energy density. This reduces the aforementioned cubic polynomial of  $\lambda^2$  to a quadratic equation of  $\lambda^2$ . Then solving the equation yields the perturbed field  $\mathbf{\Lambda}^1$  being the combination of two decaying fields.

For example, in the  $\lambda_s = 2, \alpha = 0.05$  case, the 12 non-zero second-order derivatives of the energy

$$W_N(\mathbf{\Lambda}) = W_{R2}(\mathbf{\Lambda}/\text{Det}\mathbf{\Lambda}) + B(\text{Det}\mathbf{\Lambda} - 1)^2/2 \quad (\text{S50})$$

evaluated at the base state  $\mathbf{\Lambda} = \mathbf{I} - 0.0006792\hat{\mathbf{z}} \otimes \hat{\mathbf{z}}$  are

$$\begin{cases} W_N^{((2,0,0),(0,0,0),(0,0,0))} = 100.17212, & W_N^{((1,0,0),(0,1,0),(0,0,0))} = 99.7121, & W_N^{((1,0,0),(0,0,0),(0,0,1))} = 99.7793, \\ W_N^{((0,2,0),(0,0,0),(0,0,0))} = 0.2118, & W_N^{((0,1,0),(1,0,0),(0,0,0))} = 0.2117, & W_N^{((0,0,2),(0,0,0),(0,0,0))} = 0.2121, \\ W_N^{((0,0,1),(0,0,0),(1,0,0))} = 0.2119, & W_N^{((0,0,0),(2,0,0),(0,0,0))} = 0.0100, & W_N^{((0,0,0),(0,2,0),(0,0,0))} = 99.8512, \\ W_N^{((0,0,0),(0,1,0),(0,0,1))} = 99.8985, & W_N^{((0,0,0),(0,0,0),(2,0,0))} = 0.0100, & W_N^{((0,0,0),(0,0,0),(0,0,2))} = 99.9858, \end{cases} \quad (\text{S51})$$

resulting in two perturbed fields

$$\begin{aligned} \mathbf{\Lambda}_{(1)}^1 &= 0.77817555 \exp(0.77827228z) - 0.20666114 \exp(0.77827228z) + \exp(0.77827228z), \\ \mathbf{\Lambda}_{(2)}^1 &= 2.029273 \exp(2.0298365z) - 4.6718188 \exp(2.0298365z) + \exp(2.0298365z) \end{aligned} \quad (\text{S52})$$

and the minimum eigenvalue of Hessian being  $-0.239$  at  $\theta = 0.35\pi$ .

## X. MOVIE CAPTIONS

**M1.** 85  $\mu\text{m}$  thick film cooling from the isotropic state under reflection light.

**M2.** 220  $\mu\text{m}$  thick film cooling from the isotropic state under reflection light.

**M3.** 220  $\mu\text{m}$  thick film heating and cooling cycles under transmission POM.

**M4.** 85  $\mu\text{m}$  thick film cooling from the isotropic state under transmission POM. Cross-hatch microstructure evolution is seen upon cooling.

**M5.** Simulation of the dynamics and coarsening of surface instability in a nematic elastomer.

Supporting videos can be accessed at [https://drive.google.com/drive/folders/18DCJz0DnNKFKmrJ1Ggy\\_Q40\\_UhXbj8XH?usp=sharing](https://drive.google.com/drive/folders/18DCJz0DnNKFKmrJ1Ggy_Q40_UhXbj8XH?usp=sharing)

- 
- [S1] M. Barnes and R. Verduzco, Direct shape programming of liquid crystal elastomers, *Soft Matter* **15**, 870 (2019).  
[S2] M. Warner and E. M. Terentjev, *Liquid crystal elastomers*, Vol. 120 (Oxford university press, 2007).  
[S3] S. Conti, A. DeSimone, and G. Dolzmann, Semisoft elasticity and director reorientation in stretched sheets of nematic elastomers, *Physical Review E* **66**, 061710 (2002).  
[S4] A. DeSimone and G. Dolzmann, Macroscopic response of nematic elastomers via relaxation of a class of so (3) invariant energies, *Archive for rational mechanics and analysis* **161**, 181 (2002).  
[S5] T. Tallinen, J. S. Biggins, and L. Mahadevan, Surface sulci in squeezed soft solids, *Physical review letters* **110**, 024302 (2013).  
[S6] M. Destrade, B. M. Donald, J. Murphy, and G. Saccomandi, At least three invariants are necessary to model the mechanical response of incompressible, transversely isotropic materials, *Computational Mechanics* **52**, 959 (2013).